JGR Atmospheres

RESEARCH ARTICLE
10.1029/2024JD041266

Global Fossil Methane Emissions Constrained by Multi-Isotopic Atmospheric Methane Histories

Ryo Fujita[1,2], Heather Graven[1], Giulia Zazzeri[1,3], Benjamin Hmiel[4,5], Vasilii V. Petrenko[4], Andrew M. Smith[6], Sylvia E. Michel[7], and Shinji Morimoto[8]

[1]Department of Physics, Imperial College London, London, UK, [2]Meteorological Research Institute, Japan Meteorological Agency, Tsukuba, Japan, [3]Ricerca sul Sistema Energetico (RSE), Milan, Italy, [4]Department of Earth and Environmental Sciences, University of Rochester, Rochester, NY, USA, [5]Environmental Defense Fund, New York, NY, USA, [6]Centre for Accelerator Science, Australian Nuclear Science and Technology Organisation (ANSTO), Lucas Heights, NSW, Australia, [7]Institute of Arctic and Alpine Research, University of Colorado, Boulder, CO, USA, [8]Center for Atmospheric and Oceanic Studies, Graduate School of Science, Tohoku University, Sendai, Japan

Abstract The global CH_4 budget of sources and sinks is highly uncertain, particularly the emissions from specific sources such as fossil fuels (FF) or agriculture. Here, we estimate plausible global CH_4 source and sink scenarios using historical observations and simulations of atmospheric CH_4 mole fraction and its stable isotopic ($\delta^{13}C$-CH_4, δD-CH_4) and radiocarbon ($\Delta^{14}C$-CH_4) composition, combining constraints from all these tracers for the first time. We employ a one-box model along with a Monte Carlo particle filter technique, explicitly exploring the impact of each isotopic constraints and uncertainties in prior CH_4 source and sink parameters on posterior sectorial source fractions. We find our posterior anthropogenic FF emissions at the global scale are 30% lower than previous isotope-based studies. Our analysis suggests previous $\delta^{13}C$-CH_4-based studies are potentially biased because the current database-derived estimate of the global mean biogenic $\delta^{13}C$-CH_4 source signature is too low and/or current sink-weighted total carbon kinetic isotope effect is underestimated. We find modern atmospheric $\Delta^{14}C$-CH_4 data constrains lower global FF emissions after 1980s, which is contrary to the most recent finding that utilized atmospheric $\Delta^{14}C$-CH_4 data, but supported by an independent estimate of global nuclear $^{14}CH_4$ emissions. Our multi-isotopic constraints align with CH_4-only inversion results, while reducing their uncertainties with greater robustness against different prior emission scenarios. We find strong constraints not only on FF emissions but also other key sources and sinks, showing that long-term multi-isotopic observations are critical for refining the global CH_4 budget and developing effective CH_4 emission mitigation strategies.

Plain Language Summary Reduction of methane (CH_4) emissions is a key element of climate change mitigation. However, studies using different techniques to quantify emissions from specific sources (e.g., fossil fuel (FF) or agriculture) are in conflict. Isotopic tracers are useful because different CH_4 sources have different isotopic signatures, especially radiocarbon for distinguishing between fossil and biogenic sources, but most studies have not used all data available or accounted for all relevant uncertainties in parameters related to the isotopic methane budget. Here, we synthesize all available constraints from atmospheric CH_4 concentration and its major isotopologues ($^{13}CH_4$, CH_3D, and $^{14}CH_4$) for 1750–2015, considering the relevant uncertainties, to estimate global CH_4 emissions and sinks. We find our global total emissions from the FF industry are lower than other previous isotope-based studies. Our study provides critical constraints on the global CH_4 emissions, which can support climate mitigation efforts, including the Global Methane Pledge.

Key Points:

- Bottom-up estimates of natural CH_4 emissions are too high, while bottom-up estimates of anthropogenic CH_4 emissions are not too low
- Our global total emissions from the fossil fuel industry are 30% lower than previous isotope-based studies
- Atmospheric $\Delta^{14}C$ data constrain lower anthropogenic fossil sources, consistent with a data-based estimate for nuclear $^{14}CH_4$ emissions

Supporting Information:

Supporting Information may be found in the online version of this article.

Correspondence to:

R. Fujita,
ryo.fujita@mri-jma.go.jp

Citation:

Fujita, R., Graven, H., Zazzeri, G., Hmiel, B., Petrenko, V. V., Smith, A. M., et al. (2025). Global fossil methane emissions constrained by multi-isotopic atmospheric methane histories. *Journal of Geophysical Research: Atmospheres*, *130*, e2024JD041266. https://doi.org/10.1029/2024JD041266

Received 2 APR 2024
Accepted 31 OCT 2024

1. Introduction

Atmospheric CH_4 concentration has more than doubled over the industrial era, with anthropogenic CH_4 emissions contributing ~30% to anthropogenic greenhouse gas effective radiative forcing over 1750–2019 (IPCC, 2021), while the CH_4 growth rate has varied substantially in recent years with record high growth in 2020 and 2021 (Dlugokencky et al., 2021). The partitioning of CH_4 sources and their contributions to CH_4 growth rate variations is an area of controversy and uncertainty, primarily because there is a wide range of poorly quantified anthropogenic sources (e.g., agriculture, landfills, fossil fuels (FFs)), natural sources (e.g., wetlands, freshwater, geological processes), and sinks (mainly chemical reactions with OH) (Saunois et al., 2020). The uncertainties in

the CH_4 budget limit the creation of effective mitigation policies and the prediction of future CH_4 radiative forcing.

A key question is the attribution of total fossil sources (i.e., FF industries plus natural geologic seepage) versus biogenic sources to the global CH_4 budget. Several recent studies have indicated that CH_4 emissions from the FF industry could be underestimated by bottom-up inventory estimates (e.g., Hmiel et al., 2020; Schwietzke et al., 2016). Further, atmospheric measurements have detected underestimated fugitive CH_4 emissions from FF production regions (Alvarez et al., 2018), flaring sites (Plant et al., 2022), and some urban regions (Sargent et al., 2021), as well as unexpected CH_4 "superemitters" (Lauvaux et al., 2022). However, the global significance of underestimated fugitive emissions is not yet clear.

Atmospheric isotopic analyses, which exploit differing isotopic source signatures in stable isotopes ($^{13}CH_4$ and CH_3D) and radiocarbon ($^{14}CH_4$), indicate the total fossil sources comprise 28%–33% of global emissions (Fujita et al., 2020; Lan et al., 2021; Lassey, Lowe et al., 2007; Schwietzke et al., 2016), whereas the Global Carbon Project (GCP) suggest only 21%–24% (Saunois et al., 2020). Radiocarbon is an excellent fossil CH_4 tracer because radioactive decay over millions of years removed $^{14}CH_4$ in fossil CH_4 (Lassey, Lowe et al., 2007). Ice core and firn air atmospheric $\Delta^{14}C\text{-}CH_4$ data show that natural geological emissions are small (Hmiel et al., 2020), suggesting that the vast majority of these extra fossil emissions are from the FF industry, whereas bottom-up estimates of natural geological emissions indicate they could comprise up to ~40% of total fossil emissions (Etiope & Schwietzke, 2019). Challenges with applying $\Delta^{14}C\text{-}CH_4$ data are that data are sparse and recent atmospheric $\Delta^{14}C\text{-}CH_4$ is also influenced by uncertain nuclear power plant (NPP) emissions (Lassey, Etheridge, et al., 2007; Lassey, Lowe et al., 2007). Stable isotopic approaches also exploit differences in isotopic signatures of different sources, but suffer from significant uncertainty of the major isotopic source signatures as well as OH variability and its kinetic isotope effect (KIE), leading to ambiguous source attributions (Lan et al., 2021; Rigby et al., 2017; Turner et al., 2017). Two recent $\delta^{13}C\text{-}CH_4$ inversion studies agree that uncertainties limit the application of $\delta^{13}C\text{-}CH_4$ measurements in CH_4 source attribution, but come to different conclusions: Thanwerdas et al. (2022) highlight the impact of uncertainties in $\delta^{13}C\text{-}CH_4$ source signatures on sectorial source attributions, whereas Basu et al. (2022) suggest the uncertainties in KIEs are more important than the $\delta^{13}C\text{-}CH_4$ source signatures.

Here, we synthesize all available constraints from atmospheric CH_4, $\delta^{13}C\text{-}CH_4$, $\delta D\text{-}CH_4$, and $\Delta^{14}C\text{-}CH_4$ observations for the first time to estimate plausible global CH_4 source and sink scenarios over 1750–2015. We utilize a one-box atmospheric model and a particle filter (PF) (or sequential Monte Carlo filter) approach (Doucet et al., 2001; Kitagawa, 1996) to optimize global CH_4 source and sink parameters. We derive posterior distributions of the CH_4 source strengths as well as their isotope source signatures, total CH_4 loss rate, KIEs, biospheric turnover time, and average NPP $^{14}CH_4$ emissions factor by evaluating the simulations against historical global observational target ranges. In this study, we chose a one-box model over a 3D transport model, prioritizing simplicity, computational cost, and transparency for the scope of this study. Our simple box model approach enables us to utilize not only $\delta^{13}C\text{-}CH_4$, which is relatively well sampled globally, but also $\delta D\text{-}CH_4$ and $\Delta^{14}C\text{-}CH_4$, whose spatiotemporal data coverage is still sparse and thus have not been incorporated into 3D model inversions so far. By leveraging the cheap calculation cost, we perform large ensemble simulations (100,000 realizations per each prior emission scenario) as well as many sensitivity tests to explore the impact of individual data constraints and individual uncertainties in CH_4 source and sink parameters when deriving sectorial CH_4 source emissions.

2. Methods

2.1. Model Description

We conduct numerous forward simulations of CH_4, $^{13}CH_4$, CH_3D, and $^{14}CH_4$ using a one-box model with varying parameters. Following Lassey, Etheridge, et al. (2007), simple global mass balance equations for total CH_4, $^{13}CH_4$, CH_3D, and $^{14}CH_4$ were prepared as follows:

$$\frac{dC_{\mathrm{ATM}}}{dt} = \sum_{i=1}^{N} E_{\mathrm{src}(i)} - \frac{C_{\mathrm{ATM}}}{\lambda_{\mathrm{tot}}} \quad (1)$$

$$\frac{d(C_{\mathrm{ATM}}R_{13C\_\mathrm{ATM}})}{dt} = \sum_{i=1}^{N} E_{\mathrm{src}(i)}R_{13C\_\mathrm{src}(i)} - \frac{1}{\mathrm{KIE}^{C}\lambda_{\mathrm{tot}}}C_{\mathrm{ATM}}R_{13C\_\mathrm{ATM}} \quad (2)$$

$$\frac{d(C_{\mathrm{ATM}}R_{D\_\mathrm{ATM}})}{dt} = \sum_{i=1}^{N} E_{\mathrm{src}(i)}R_{D\_\mathrm{src}(i)} - \frac{1}{\mathrm{KIE}^{D}\lambda_{\mathrm{tot}}}C_{\mathrm{ATM}}R_{D\_\mathrm{ATM}} \quad (3)$$

$$\frac{d(C_{\mathrm{ATM}}R_{14C\_\mathrm{ATM}})}{dt} = \sum_{i=1}^{N} E_{\mathrm{src}(i)}R_{14C\_\mathrm{src}(i)} + \phi W_{\mathrm{PWR}} - \left(\left(\frac{1}{\mathrm{KIE}^{C}}\right)^{2}\frac{1}{\lambda_{\mathrm{tot}}} + \frac{1}{\lambda_{\mathrm{r}}}\right)C_{\mathrm{ATM}}R_{14C\_\mathrm{ATM}} \quad (4)$$

where C_{ATM} is the atmospheric burden of total CH_4; R_{13C}, R_D, and R_{14C} denote the absolute stable carbon, hydrogen, and radiocarbon isotope ratios (i.e., $^{13}CH_4$/total CH_4, CH_3D/total CH_4, and $^{14}CH_4$/total CH_4), respectively, of atmosphere (ATM) and respective source categories (src); E indicates the global CH_4 emissions of respective source categories; N is the number of source categories, equal to five, consisting of anthropogenic biogenic (BIO), natural BIO, anthropogenic FF, geologic (GEO), and biomass burning (BB) sources; λ denotes the atmospheric lifetime for total CH_4 sink processes (tot) and radioactive decay (r); KIE^{C} and KIE^{D} are the sink-weighted total KIEs for stable carbon and hydrogen isotopes, respectively; and ϕW_{PWR} represents the direct NPP $^{14}CH_4$ emissions where W_{PWR} is the annual electrical power production by pressurized water reactors (PWR) and ϕ is the $^{14}CH_4$ emissions per annual electrical power production (i.e., NPP $^{14}CH_4$ emission factor) (GBq/GWa). The atmospheric $^{13}CH_4$, CH_3D, and $^{14}CH_4$ are convertible to δ^{13}C-CH_4, δD-CH_4, and Δ^{14}C-CH_4, respectively (Text S1 in Supporting Information S1).

We prepared three alternative a priori global CH_4 emission scenarios for 1750–2015 using three different anthropogenic emission inventories: Community Emissions Data System (CEDS) (Hoesly et al., 2018; prepared for Coupled Model Intercomparison Project Phase 6 (CMIP6), v2017-05-18) and Emissions Database for Global Atmospheric Research version 5.0 and 6.0 (EDGARv5 and EDGARv6) (Crippa et al., 2020, 2021). We used the same a priori estimates of BB, natural BIO, and GEO CH_4 sources in all scenarios (Table S2 in Supporting Information S1). For the CEDS scenario, we adopted the global sectorial anthropogenic CH_4 emissions for CEDS for 1850–2014 (decadal until 1970 and yearly afterward). For the EDGAR scenarios, we reconstructed the historical emissions using EDGAR-HYDE v1.4 for 1890–1960 (decadal) (Olivier & Berdowski, 2001; van Aardenne et al., 2001), and combined it with EDGARv5.0 or EDGARv6.0 for 1970–2015 (yearly). The a priori anthropogenic CH_4 emissions in 1750 were specified from Lassey, Etheridge, et al. (2007) for each source category, the CH_4 emissions for EDGAR in 1850 were specified by CEDS, and the CH_4 emissions for CEDS in 2015 were specified by Gidden et al. (2019). To keep the data consistency where annual data were unavailable, each source emission was linearly interpolated using the adjacent available data. For BB CH_4 emissions, the annual mean historical global emission data set for CMIP6 (BB4CMIP) (van Marle et al., 2017) over 1750–2015 was used for all three scenarios. We included residential, commercial, and other sectors (called "RCO" in CEDS or "1.a.d Other sectors" in EDGAR) into anthropogenic FF emissions, assuming this combustion was from FFs. A sensitivity test was performed to investigate the impact of this choice (RCOem; Table S3 in Supporting Information S1). Time-invariant a priori natural CH_4 emissions (e.g., wetland, freshwater, and GEO) were taken from bottom-up averages for 2000–2009 (Saunois et al., 2020) (Table S2 in Supporting Information S1). Sensitivity tests were also performed for different a priori interannually varying natural wetland emission scenarios (IAWetBIOem; Table S3 in Supporting Information S1). Emissions from freshwater systems vary widely between bottom-up and top-down estimates (134–284 Tg CH_4 yr^{-1} vs. less than 30 Tg CH_4 yr^{-1}; Saunois et al., 2020); thus, a scenario excluding freshwater emissions were also examined in a sensitivity test (NoFRESHem; Table S3 in Supporting Information S1).

Our a priori atmospheric total CH_4 lifetime is based on Prather et al. (2012) (9.1 ± 0.9 years), which is constrained by atmospheric methyl chloroform (MCF) for tropospheric OH and literature-based estimates for the other sinks (i.e., soil oxidations, stratospheric losses, and tropospheric Cl). To consider the potential time evolutions of atmospheric OH into Prather et al., 2012's scenario, we applied an ensemble mean anomaly (relative to the 1998–2007 mean) of global OH computed by Earth System Models (ESMs) that participated in the CMIP6 (Stevenson et al., 2020) to the loss rate of tropospheric CH_4-OH reactions in Prather et al. (2012). The prior OH anomaly from Stevenson et al. (2020) used in our base simulation shows little changes from 1850 to 1980, followed by strong increases by 9% through 2014. In contrast, recent MCF-based OH shows downward trends by about 8% since

2005 (Rigby et al., 2017; Turner et al., 2017) or rather stable trends since 2000 (Naus et al., 2021; Patra et al., 2021), the latter being consistent with the empirical reconstruction estimate (Nicely et al., 2018). We therefore tested the sensitivity of different prior OH scenarios for the recent decades as time-invariant or from recent MCF-based estimates (OHtrend; Table S3 in Supporting Information S1). Note that because we did not explicitly simulate different loss processes in the model (see Equations 1–4), such time variations of tropospheric OH need to be interpreted as those of total loss rates after the sink fractions in Prather et al. (2012) is applied.

The W_{PWR} were taken from Lassey, Etheridge, et al. (2007) for 1960–1971 and assumed to be zero before 1960. For 1972–2015, the database of annual energy output for PWRs from International Atomic Energy Agency's Power Reactor Information System (IAEA PRIS, 2017) was used. The absolute radiocarbon isotope ratio of biospheric (i.e., BIO and BB) sources, R_{14C_bios}, was calculated following Lassey, Etheridge, et al. (2007) as follows:

$$R_{14C\_bios}(t) = \int_0^\infty \left(1 + \Delta^{14}CO_2(t - t')/1000\right) F(t') \exp\left(-\lambda_r t'\right) dt' \quad (5)$$

$$F(t') = \frac{\exp\left(-t'/\tau_{bios}\right)}{\tau_{bios}} \quad (6)$$

where $\Delta^{14}CO_2$ is the time series of atmospheric $\Delta^{14}C\text{-}CO_2$, $F(t')$ is an exponential distribution of lag times (i.e., the residence time of the biospheric carbon before it is released as CH_4), and τ_{bios} is the mean biospheric turnover time. Historical global atmospheric $\Delta^{14}C\text{-}CO_2$ observations were taken from Graven et al. (2017) over 1850–2015 (yearly) and Reimer et al. (2013) before 1850. λ_r is set to be 8,267 years. R_{14C_bios} was simulated for τ_{bios} of 1–12 years with 1-year increments over 1750–2015, and then interpolated for fractional year values of τ_{bios}.

2.2. Particle Filter Approach

We used the particle filter (PF) approach based on a Monte Carlo (MC) method for non-Gaussian nonlinear filtering and smoothing (Doucet et al., 2001; Kitagawa, 1996) to estimate the posterior distributions of 20 parameters in CH_4 sources and sinks—the scaling factors, which adjust the prior CH_4 emissions and loss rates (f), $\delta^{13}C$ and δD source signatures, KIE^C, KIE^D, τ_{bios}, and ϕ (Table 1 and Equations 1–6)—over 1750–2015. In the PF, conditional probability density functions are approximated by successive prediction and filtering of many realizations of the state variables (hereafter called "*ensembles*"). Each ensemble is propagated in time according to the model equations (Equations 1–4) with the 20 parameters (i.e., *prediction*). The ensemble is compared to observations and either accepted or rejected using the likelihood function of the observations (i.e., *filtering*). The prediction and filtering stage is repeated until the final observation target year, 2015, and finally a time series of posterior parameter distributions that match all the observation targets from 1750 to 2015 is extracted (i.e., *smoothing*). For the base simulation, we adopted 100,000 realizations for each emission scenario, which were separated into 50 sets of 2,000 ensembles to utilize a parallel computational technique.

The details of the PF procedure are described as follows. First, initial ensembles of the 20 parameters were randomly generated from their full initial ranges using Latin hypercube sampling. The first target year, 1750, was then compared to a 50-year spin-up simulation where all parameters were prescribed to be constant at the initial values (see Text S1 in Supporting Information S1 for more details). From 1750, each ensemble of the 20 parameters, $\boldsymbol{\theta}$, is assumed to follow a random walk model $\boldsymbol{\theta}_t = \boldsymbol{\theta}_{t-1} + \boldsymbol{u}_t$, where t represents a time step consisting of 51 target years over 1750–2015 (Table S1 in Supporting Information S1), and $\boldsymbol{u}_t$ is assumed to follow Gaussian distributions. Potential time variation in parameters after 1750 is thus included by resampling the accepted parameters with adding Gaussian noise u_t whose standard deviation is α% of the initial parameter ranges, where α is also estimated by the PF for each parameter of each target year. The prior distribution of α is assumed to be uniform whose upper and lower bounds are set to be [0, 10], except time-invariant parameters (geological source parameters, E_{geo}, $\delta^{13}C_{geo}$, and δD_{geo}), whose α is fixed at 0.3. A sensitivity test was performed to investigate the impact of setting all isotopic parameters to be time-invariant (IsoParaFixT; Table S3 in Supporting Information S1). The parameter values for the period between the adjacent target years are linearly interpolated. When the predicted θ_t exceeds the upper or the lower bound of the initial prior parameter ranges (Table 1), the θ_t is replaced by θ_{t-1} to avoid divergence from prior knowledge.

Table 1
Summary of 20 Parameters and Their Ranges Used in Our Base Simulation

Parameter	Mean [min., max.]	Definition
f_{anth_bio}	1.0 [0.5, 1.5][a, b, c]	Scaling factor that adjusts the prior anthropogenic BIO CH_4 emission
f_{natr_bio}	1.0 [0.5, 1.5][a, b, c]	Scaling factor that adjusts the prior natural BIO CH_4 emission
f_{anth_ff}	1.0 [0.5, 1.5][a, b, c]	Scaling factor that adjusts the prior anthropogenic FF CH_4 emission
f_{bb}	2.0 [0.5, 3.5][a, b, c]	Scaling factor that adjusts the prior BB CH_4 emission
E_{geo}	40 [0, 80][d, e]	GEO CH_4 emission (Tg CH_4 yr^{-1})
τ_{bios}	6.5 [1, 12][f]	Biospheric turnover time (year)
ϕ	230 [80, 380][g]	NPP $^{14}CH_4$ emission factor (GBq/GWa)
f_{loss}	1.0 [0.9, 1.1][h]	Scaling factor that adjusts the prior total CH_4 loss rate
KIE^C	1.0065 [1.005, 1.008][a, b]	Sink-weighted total KIE^C
KIE^D	1.275 [1.25, 1.30][a, b]	Sink-weighted total KIE^D
$\delta^{13}C_{anth\_bio}$	−62.2 [−65.4, −59.0][a]	$\delta^{13}C$-CH_4 for anthropogenic BIO source (‰)
$\delta^{13}C_{natr\_bio}$	−62.2 [−65.4, −59.0][a]	$\delta^{13}C$-CH_4 for natural BIO source (‰)
$\delta^{13}C_{anth\_ff}$	−44.0 [−46.8, −41.2][a]	$\delta^{13}C$-CH_4 for anthropogenic FF source (‰)
$\delta^{13}C_{bb}$	−22.2 [−29.8, −14.6][a]	$\delta^{13}C$-CH_4 for BB source (‰)
$\delta^{13}C_{geo}$	−49.0 [−52.0, −46.0][i]	$\delta^{13}C$-CH_4 for GEO source (‰)
δD_{anth_bio}	−317 [−332, −302][j]	δD-CH_4 for anthropogenic BIO source (‰)
δD_{natr_bio}	−317 [−332, −302][j]	δD-CH_4 for natural BIO source (‰)
δD_{anth_ff}	−197 [−212, −182][j]	δD-CH_4 for anthropogenic FF source (‰)
δD_{bb}	−211 [−226, −196][j]	δD-CH_4 for BB source (‰)
δD_{geo}	−197 [−212, −182][j]	δD-CH_4 for GEO source (‰)

[a]Schwietzke et al. (2016). [b]Fujita et al. (2020). [c]Saunois et al. (2020). [d]Etiope and Schwietzke (2019). [e]Hmiel et al. (2020). [f]Lassey, Etheridge, et al. (2007). [g]Graven and Gruber (2011). [h]Prather et al. (2012). [i]Etiope et al. (2019). [j]Sherwood et al. (2017).

For each prediction stage, the number of ensembles was amplified by 10; that is, 2,000 × 10 ensembles were generated at each target year for each 50 parallel computation. This is effective to avoid "particle degeneracy"—when only a small number of ensembles has a nonzero importance weight through the filtering and thus the PF approach fails to accurately reproduce the posterior distributions of interest (Doucet et al., 2001). The log likelihood of each of the 20,000 ensembles in each parallel computation was calculated, and 2,000 new ensembles were created based on the likelihood and sequential importance sampling with replacement (Doucet et al., 2001; Kitagawa, 1996). The likelihood of each ensemble was computed based on the prescribed observation targets (Table S1 in Supporting Information S1). After the filtering stage in 2015, the filtered ensembles at each time step were sequentially resampled from the stored likelihood to obtain the conditional joint distribution for all time steps. Thus, a time series of posterior parameter distributions that match all the observation targets for 1750–2015 were extracted (see Kitagawa, 1996; Doucet et al., 2001 for more details).

2.3. Parameters in CH_4 Sources and Sinks

Table 1 shows a summary of the 20 parameters in CH_4 sources and sinks. Because our prior knowledge on source and sink parameters is uncertain, we specified all parameter ranges to be quite wide in recognition of their uncertainties and realistic boundaries. We assumed that applying a subjective prior mean and standard deviation in prior Gaussian distributions extrapolated from current limited observational evidence (e.g., prior isotopic source signatures during a historical period) could introduce biases in their posterior estimates. As a compromise, we applied an initial uniform distribution with wide upper and lower bounds of each parameter, which were estimated from the literature (Table 1), and then utilized our atmospheric observational target to progressively optimize the parameters (see Section 3.1).

The scaling factors, which adjust the prior anthropogenic BIO, natural BIO, and anthropogenic FF CH_4 emissions (f_{anth_bio}, f_{natr_bio}, and f_{anth_ff}, respectively), were set to be 1.0 [0.5, 1.5] (mean and minimum–

maximum range), and that for BB CH_4 emissions (f_{bb}) to be 2.0 [0.5, 3.5]. They were approximately lower and upper bounds of previous estimates of top-down and bottom-up CH_4 emissions when these scaling factors were applied to our prior emissions (Fujita et al., 2020; Saunois et al., 2020; Schwietzke et al., 2016). For geologic CH_4 emissions (E_{geo}), the range was set to be 40 [0, 80] Tg CH_4 yr^{-1}. The lower bound was taken from the atmospheric $\Delta^{14}C$-CH_4-based estimate (Hmiel et al., 2020), whereas the mean and upper bound was taken from the current bottom-up estimate (Etiope & Schwietzke, 2019). The range in mean biospheric turnover time (τ_{bios}) was set to be 6.5 [1, 12], which was taken from the best estimate of Lassey, Etheridge, et al. (2007) but with larger uncertainty. The range of NPP $^{14}CH_4$ emission factor (ϕ), 230 [80, 380], was adopted from a 70% confidence interval (CI) of the total PWR ^{14}C emissions from Graven and Gruber (2011) after multiplying it by 72% to extract $^{14}CH_4$ emissions only (Zazzeri et al., 2018). The range of ϕ covers the previous observation-based estimates in Kunz (1985) and Eisma et al. (1995).

The scaling factor for the total CH_4 loss rate (f_{loss}) was set to be 1.0 [0.9, 1.1], following ± 1 SD of Prather et al. (2012). The prior mean of total KIE^C and KIE^D were set to be the same as Fujita et al. (2020) (1.0065 and 1.275) and similar to Schwietzke et al. (2016) for KIE^C (1.0063), so as to directly compare our results with the two isotopic modeling studies. The prior sink-weighted total KIE^C and KIE^D ranges were set to be [1.005, 1.008] and [1.25, 1.30], respectively, based on average sink fractions in Saunois et al. (2020) with tropospheric Cl sink of 3–11 Tg/yr and their experimental KIEs from the literature (Table S4 in Supporting Information S1). The mean $\delta^{13}C$-CH_4 and δD-CH_4 isotopic signatures for each source were taken from database-derived estimates in Schwietzke et al. (2016) and Sherwood et al. (2017), respectively, except $\delta^{13}C_{geo}$ taken from Etiope et al. (2019). Despite characterizing global mean source signatures by Schwietzke et al. (2016) and Sherwood et al. (2017), it is known that their database tends to be spatially biased—a large part of the data set was sampled in North America and only a few data were available in the tropics, especially for nonfossil sources (see Figure 2 of Sherwood et al., 2017). Because this spatial bias has not changed dramatically in their updated database (Sherwood et al., 2021), in which they did not report global mean signatures, here, we refer to Schwietzke et al. (2016) and Sherwood et al. (2017) as current database-driven global mean signatures. We thus set the uncertainty ranges of isotopic source signatures quite wide, ±4 SD of Schwietzke et al. (2016) for $\delta^{13}C$-CH_4 and ±15 permil for δD-CH_4. Mean values of each parameter range (Table 1) were used when performing prior atmospheric simulations, as presented in Figure 1.

Sensitivity tests were performed to investigate the impact of these parameter choices (ParaRange; Table S3 in Supporting Information S1). A wider prior KIE^C range [1.005, 1.010] was applied to consider potential maximum tropospheric Cl contributions (Table S4 in Supporting Information S1; with tropospheric Cl sink of 35 Tg/yr) (ParaRange #5). Many sensitivity tests were also performed by applying different ranges of specific isotopic parameters or by fixing the parameters as perfectly known parameters (ParaRange #1–4, #6–13). The impact of prior ranges of source scaling factors was also examined (ParaRange #14 and #15).

2.4. Observation Targets

We set atmospheric CH_4, $\delta^{13}C$-CH_4, δD-CH_4, and $\Delta^{14}C$-CH_4 observational target ranges for 51 target years: 1750, 1850, 1900, 1950, 1960, and every year for 1970–2015 (Figure 1, Figure S1 and Table S1 in Supporting Information S1). The target years were chosen to cover the general features of global means and trends over 1750–2015 with a discrete time space. Similar to parameter ranges, all observational ranges were specified to be quite wide in recognition of the uncertainty in the observations, especially during the early historical period, considering their global representativeness. Due to the limited spatiotemporal coverage of atmospheric observations, especially for δD-CH_4 and $\Delta^{14}C$-CH_4, we adopted multidecadal blocks of all observational targets before 1970.

The CH_4 observation targets were taken from Meinshausen et al. (2017), a historical global CH_4 data set combining Law Dome and NEEM Greenland ice core data for 1750–1983, and from NOAA Global Monitoring Laboratory (NOAA/GML) CH_4 data for 1984–2015 (Dlugokencky et al., 2021). The observational targets for 1750–2015 were specified as Gaussian distributions with means and 1 SD uncertainties. Uncertainties of 20 ppb for 1750–1950, of 10 ppb for 1960–1984, and of 5 ppb after 1984 were prescribed, considering the uncertainties of age of air in ice core data before 1984, in sample measurements, and in reconstruction of global annual means.

Because there is no representative historical global mean data set for $\delta^{13}C$-CH_4 before 1984, and δD-CH_4 and $\Delta^{14}C$-CH_4 over 1750–2015, we reconstructed these using available data sets (Ferretti et al., 2005; Fujita et al., 2020; Hmiel et al., 2020; Lassey, Etheridge, et al., 2007; Michel et al., 2021; Mischler et al., 2009; Rice et al., 2016; Schaefer et al., 2016; White et al., 2016) (see Figure S1 and Text S1 in Supporting Information S1).

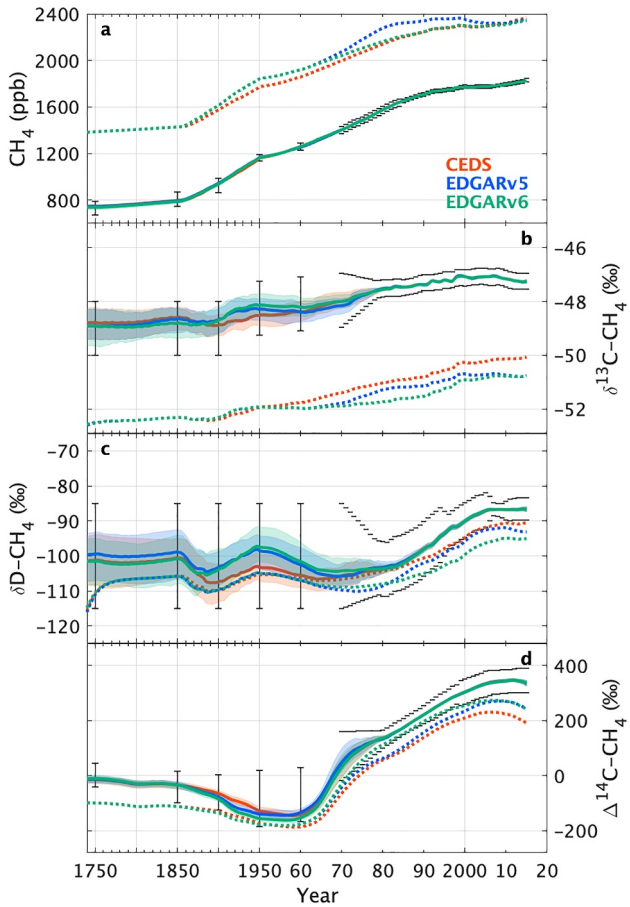

Figure 1. Simulated atmospheric CH_4 and isotopic histories compared to observation-based target ranges. Time series of simulated atmospheric CH_4 (a), δ^{13}C-CH_4 (b), δD-CH_4 (c), and Δ^{14}C-CH_4 (d) are presented in CEDS (red), EDGARv5 (blue), and EDGARv6 (green) prior and posterior scenarios over 1750–2015. Posterior mean values are shown in solid lines, and colored bands mark the 68% CI (given by 16th and 84th percentiles), which are available in Dataset S1. Dotted lines show prior mean values. Black bars show prescribed global observational target ranges (cap only after 1970). Observations and target ranges are also shown in Figure S1 and Table S1 in Supporting Information S1. Note the time axis before 1950 is rescaled.

Only upper and lower bounds of their global means were prescribed as observation targets until 1978 for δ^{13}C-CH_4 and δD-CH_4 and until 1979 for Δ^{14}C-CH_4 using available ice/core firn data (Ferretti et al., 2005; Hmiel et al., 2020; Lassey, Etheridge, et al., 2007; Mischler et al., 2009). This was due to the limited number of data, as well as limited time and space representativeness of these observations over the period (Text S1 in Supporting Information S1). After the 1970s, the global means and 1 SD uncertainties of δ^{13}C-CH_4, δD-CH_4, and Δ^{14}C-CH_4 were specified. For 1978–1983, the northern composite δ^{13}C-CH_4 data set in Rice et al. (2016) was utilized to reconstruct annual global averages. Subsequently, annual mean globally averaged δ^{13}C-CH_4 for 1984–2013 combining the Institute of Arctic and Alpine Research (INSTAAR)/NOAA for 1999–2013 (Michel et al., 2021) and the National Institute of Water and Atmospheric Research (NIWA) for 1984–1998 (Schaefer et al., 2016), compiled in Schwietzke et al. (2016), were used. The uncertainties of the global δ^{13}C-CH_4 averages were prescribed to be 0.1‰ since 1984, as used in Schwietzke et al. (2016). For δD-CH_4, the northern composite δD-CH_4 data set in Rice et al. (2016) was also utilized to reconstruct global averages for 1978–2005, followed by global averages estimated based on global air sampling networks (Fujita et al., 2020; Rice et al., 2016; White et al., 2016). For Δ^{14}C-CH_4, the annual mean global averages were constructed using the ice/core firn data set for Δ^{14}C-CH_4 (Hmiel et al., 2020). The mean and uncertainties of global δD-CH_4 and Δ^{14}C-CH_4 averages were estimated based on MC simulations (see Text S1 in Supporting Information S1 for more details). The mean and uncertainty of targets, for which the values were not prescribed, were linearly interpolated using the adjacent data.

We assumed the atmospheric burden is directly proportional to the global mean surface mole fractions at 2.75 Tg CH_4 ppb^{-1} (Prather et al., 2012). This includes the ratio of the integrated burden of the observed vertical profile of CH_4 mole fractions (i.e., surface to stratosphere) relative to that if it were uniformly mixed throughout the atmosphere, the value being 0.973 (Prather et al., 2012). Here, we also applied the same conversions for $^{13}CH_4$, CH_3D, and $^{14}CH_4$, as done in previous box model studies (e.g., Lassey, Etheridge, et al., 2007; Schwietzke et al., 2016), although stratospheric δ^{13}C-CH_4, δD-CH_4, and Δ^{14}C-CH_4 differs from the surface values. However, because the amount of CH_4 in the stratosphere is much lower than in the troposphere, we confirmed the impact of these differences are within the limits of the uncertainties we consider and therefore do not affect our conclusion (Text S1 in Supporting Information S1).

Sensitivity tests were performed to investigate the impact of each atmospheric isotopic observational constraint by applying different combinations of observational constraints (Obs; Table S3 in Supporting Information S1). The impact of potential interlaboratory differences of isotopic measurements was also examined (ObsIsoILD; Table S3 in Supporting Information S1).

While the use of the one-box model removes information contained in spatial gradients, we chose to follow this approach based on the sparse data coverage and the computational efficiency of the one-box model for exploring many parameter uncertainties and sensitivity tests. The limitations of our one-box model approach are discussed further in Section 4.3.

2.5. Observational Estimates of Global Nuclear Power Plant $^{14}CH_4$ Emission Factor

Based on the European RAdioactive Discharges Database (RADD, 2017) of ^{14}C emissions and the IAEA PRIS database of nuclear power generation (IAEA PRIS, 2017), Zazzeri et al. (2018) calculated global $^{14}CH_4$ emissions from PWRs for the period of 1972–2016 by applying the observed lognormal emission factor distributions for

PWRs in 600 MC simulations to global power generation data. In this study, we updated their results by applying several changes: (a) The data from France, reported in RADD (2017), were excluded from the analysis due to their constant emission factors, suggesting that these values may not have been derived from empirical measurements. (b) Separate observation-based lognormal distributions were used for the Soviet-design VVER reactors (Zazzeri et al., 2018) (−0.90 and 0.29 for the log of the mean and standard deviation, respectively, in TBq/GWa) and for all other PWR reactors (−1.65 and 0.93). (c) A fraction of ^{14}C released as non-CO_2 from the PWRs was estimated based on the measurements of total ^{14}C and $^{14}CO_2$ emissions from each 20 reactors reported in RADD averaged for 1995–2015 (mean: 75%, min: 44%, and max: 95%), not fixed at 72% as in Zazzeri et al. (2018). (d) The organic fraction of ^{14}C released as non-CO_2 from PWRs that is $^{14}CH_4$ was assumed to be a uniform distribution ranging 68%–77%, based on earlier measurements of organic ^{14}C species in PWRs (Kunz, 1985), not 100% as in Zazzeri et al. (2018). (e) The total MC simulation number was set to be 10,000, not 600 in Zazzeri et al. (2018). We thus conducted new MC simulations including these changes and estimated the $^{14}CH_4$ NPP emission factors (ϕ) and their 95% CI (given by 2.5th and 97.5th percentiles).

3. Results

3.1. Global CH_4 Emissions, Sinks, and Parameters

Figure 1 shows simulated atmospheric CH_4, $\delta^{13}C$-CH_4, δD-CH_4, and $\Delta^{14}C$-CH_4 under our base simulation, compared to the observation-based target ranges. The posterior parameter ensembles reproduce observed atmospheric histories well, whereas the prior mean scenarios do not match observations. The prior scenarios differ by using CEDS, EDGARv5.0, or EDGARv6.0 for anthropogenic emissions but otherwise share the same emissions, sink, and parameters. In the prior scenarios, there are large overestimations of CH_4 and underestimations of $\delta^{13}C$-CH_4, whereas the observed trends of δD-CH_4 and $\Delta^{14}C$-CH_4 are generally captured but with slight underestimations, particularly in $\Delta^{14}C$-CH_4. These discrepancies are resolved with plausible combinations of optimized parameters that reproduce all the atmospheric CH_4 tracers simultaneously in the posterior ensembles (Figure 1).

The time series of the posterior 20 parameter ensembles in CEDS, EDGARv5, and EDGARv6 scenarios are shown in Figure 2. Histograms of these parameters averaged for the period 2003–2012 are shown in Figure 3. As described in Section 2.3, the prior initial distributions of all these parameters (corresponding to the vertical axis range in Figure 2 and gray lines in Figure 3) were specified to be quite wide. Despite the weak prior constraints, the posterior distributions of f_{bb}, f_{anth_bio}, f_{natr_bio}, f_{anth_ff}, E_{geo}, ϕ, τ_{bios}, f_{loss}, KIE^C, KIE^D, $\delta^{13}C_{anth\_bio}$, $\delta^{13}C_{natr\_bio}$, and $\delta^{13}C_{anth\_ff}$ are narrowed down from the prior whereas $\delta^{13}C_{geo}$, $\delta^{13}C_{bb}$, δD_{anth_bio}, δD_{natr_bio} δD_{anth_ff}, δD_{geo}, and δD_{bb} are not changed so much (Figure 3), indicating the different importance of each parameter for reproducing atmospheric observations under our model settings. f_{anth_bio} and f_{anth_ff} are independently optimized against three prior anthropogenic emission scenarios (Figures 2b and 2d), such that the scaling factors do not correspond to the same emissions totals, whereas the other parameters are optimized from the same priors for all scenarios.

Much lower f_{natr_bio} and E_{geo} than their prior means are consistent across the scenarios (Figures 2c and 2e). The posterior f_{bb} shows that posterior BB emissions up to 3 times larger than in the prior (van Marle et al., 2017) until 1980 and 2 times larger in the 2000s, which is also consistent across the three scenarios (Figure 2a). The posterior f_{loss} shows a slight upward shift from the prior mean until the late 1980s, followed by a gradual decrease until 2015 (Figure 2h), which slightly weakens the prior increasing OH trend since 1980 (see Section 2.1). For isotopic parameters, posterior BIO $\delta^{13}C$-CH_4 source signatures ($\delta^{13}C_{anth\_bio}$ and $\delta^{13}C_{natr\_bio}$) and KIE^C are higher than their prior means (Figures 2i–2l and 3i–3l). Slightly higher $\delta^{13}C_{anth\_ff}$ and KIE^D and lower τ_{bios} from their prior means are also obtained (Figures 2g–2j, 2m, and 3g–3j and 3m). The posterior mean ϕ is consistent with its prior mean, but with significantly narrowed distributions after late 1980 (Figures 2f and 3f).

To show how the posterior distributions change over time as atmospheric constraints filter the ensembles, the histograms of the 20 parameters for the EDGARv6 scenario in the filtering stage of selected target years are shown in Figure 4 (for 1750–1960) and Figure 5 (for 1970–2010). Already in 1750, E_{geo}, f_{natr_bio}, f_{bb}, f_{loss}, $\delta^{13}C_{natr\_bio}$, KIE^C, and KIE^D are optimized from the prior setting based on the atmospheric target in 1750 (Figures 4a–4c 4e, 4h–4j, and 4l). After 1900, f_{anth_bio}, f_{anth_ff}, and $\delta^{13}C_{anth\_bio}$ are optimized as anthropogenic emissions become larger (Figures 4b–4d and 4k). τ_{bios} is optimized after 1960 when biospheric $^{14}CH_4$ emissions increase rapidly after nuclear bomb testing (Graven et al., 2017) (Figure 4g). The NPP emission factor, ϕ, is

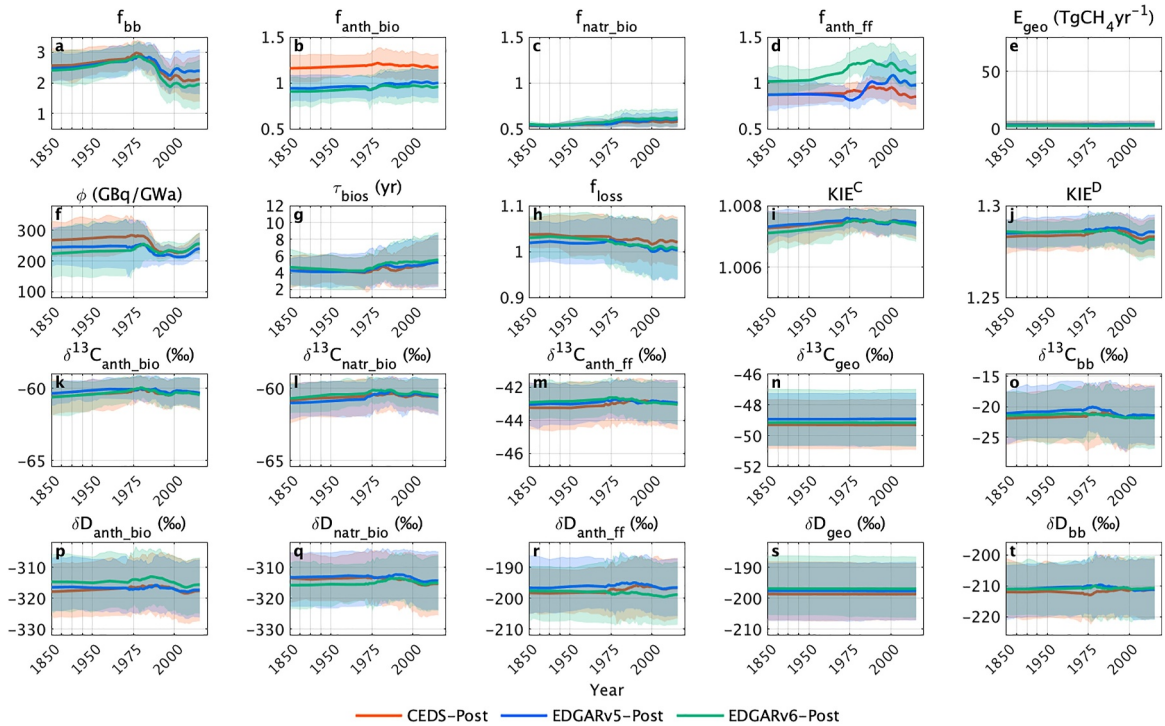

Figure 2. Time series of posterior 20 parameter ensembles in CEDS (red), EDGARv5 (blue), and EDGARv6 (green) scenarios for 1850–2015 under the base simulation. Posterior mean values are shown in solid lines, and colored bands mark the 68% CI. Each vertical axis range represents the initial prior range of that parameter.

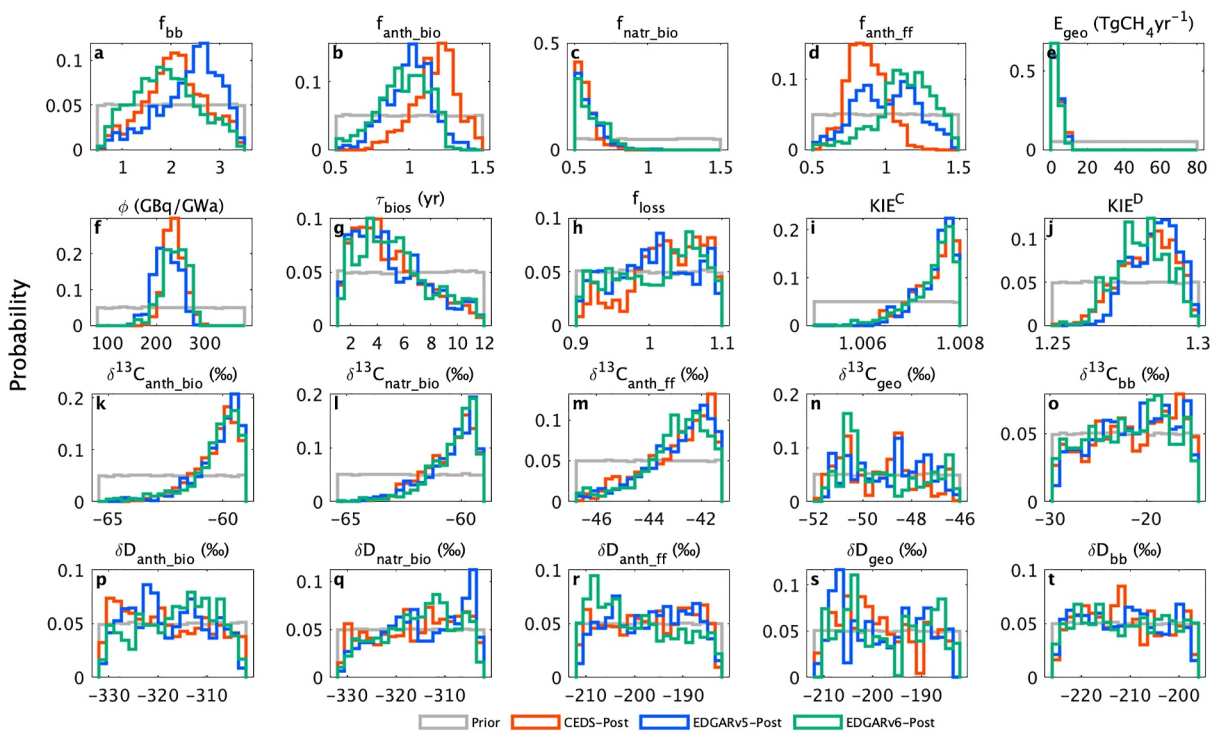

Figure 3. Histograms of posterior 20 parameter ensembles in CEDS (red), EDGARv5 (blue), and EDGARv6 (green) scenarios averaged for the period 2003–2012 under the base simulation. Also shown are their initial uniform prior distributions (gray).

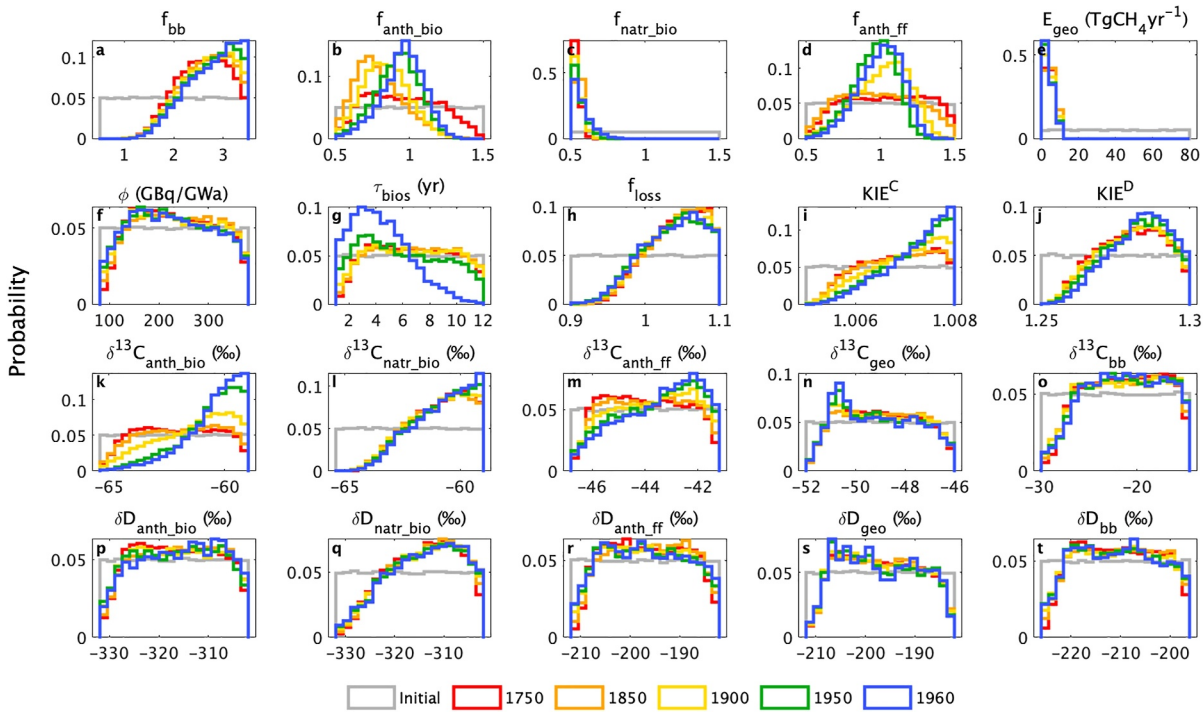

Figure 4. Same as Figure 3, but shown for the initial prior distributions and the distribution in the filtering stage of selected target years, 1750, 1850, 1900, 1950, and 1960. Here, results of only the EDGARv6 scenario are presented. See Figure 5 for subsequent target years.

optimized after the late 1980s when NPP $^{14}CH_4$ emissions rise due to the installation and increased power production of NPPs (Zazzeri et al., 2018) (Figure 5f). The $^{14}CH_4$ emissions from BIO sources after the 1950s and then from NPPs after the 1980s are reflected in the observed atmospheric trends in $\Delta^{14}C\text{-}CH_4$ (Figure 1d) (Lassey, Etheridge, et al., 2007). These results show that several parameters are sensitive to the specific observations in

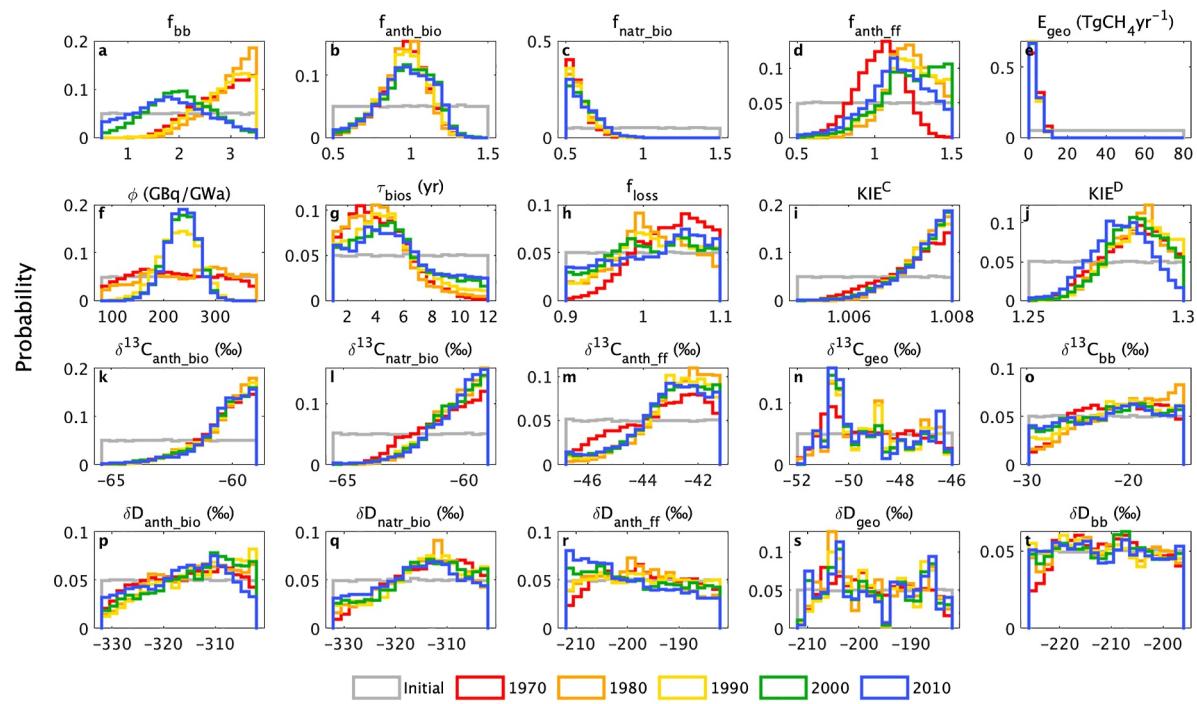

Figure 5. Same as Figure 4, but for selected target years of 1970, 1980, 1990, 2000, and 2010.

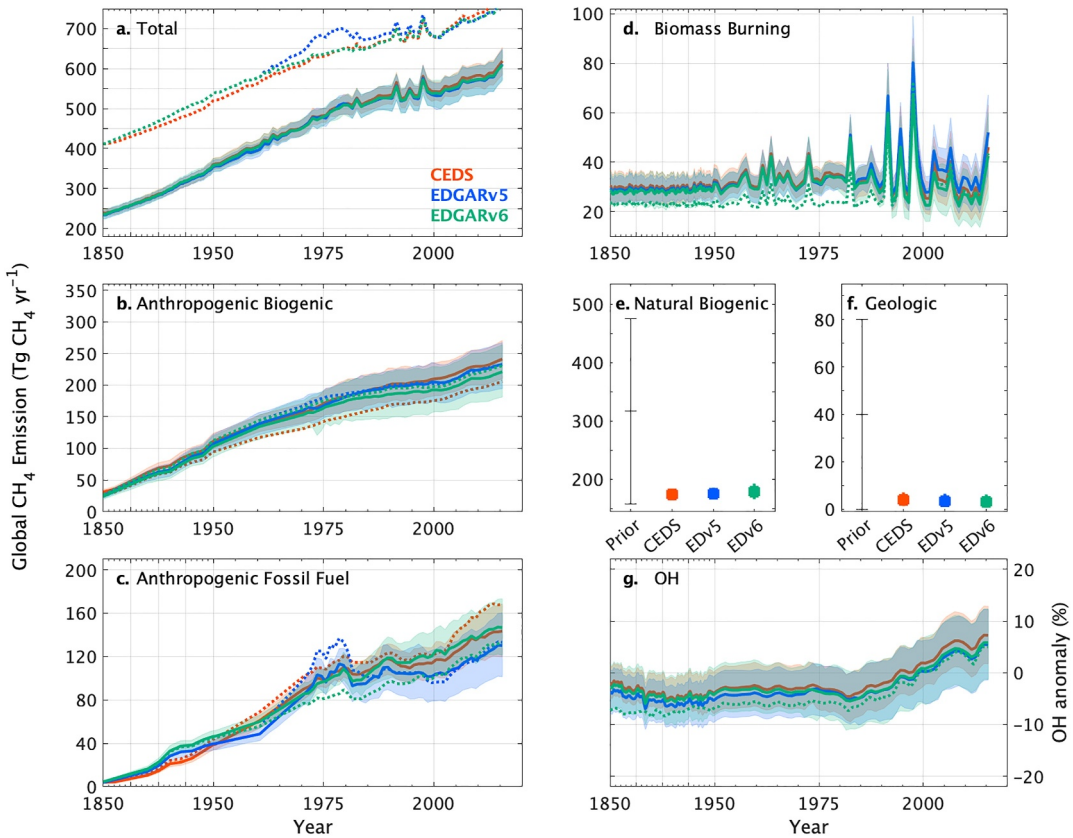

Figure 6. Prior and posterior CH_4 emissions and sinks by sectors for 1850–2015. Time series of global total (a), anthropogenic biogenic (b), anthropogenic fossil fuel (c), and biomass burning CH_4 emissions (d), and tropospheric OH anomaly (g) as well as averaged natural biogenic (e) and geologic (f) CH_4 emissions. The OH anomaly is derived from the product of our prior OH anomaly taken from Stevenson et al. (2020) (dotted line in Figure 6g) and our posterior f_{loss}. Color and line styles in panels (a–d and g) are same as Figure 1. Markers and error bars in panels (e, f) represent mean values and 68% CI, but for the mean values and full range in prior. Details of prior emissions and parameter setting are presented in Table S2 in Supporting Information S1 and Table 1, respectively.

different periods, and that not all 20 parameters are simultaneously optimized in each target period (i.e., not all parameters are necessarily correlated).

Figure 6 shows the time series of the posterior global CH_4 emissions and sinks in units of Tg CH_4 yr^{-1}, which allows an easier comparison between the different scenarios and evaluation in the context of the global CH_4 budget. Posterior anthropogenic FF emissions are not significantly higher than the prior emissions from the bottom-up inventories, except for EDGARv6 in the 1970s (Figure 6c). The posterior FF emissions from the three scenarios are consistent with each other and significantly lower than the prior emissions in EDGARv5 in the 1970s and CEDS after 2002 (Figure 6c). The rapid growth in the 1970s in EDGARv5, driven by the Middle East and Africa (i.e., oil producing countries), appears to be revised downward too strongly in the newer version EDGARv6, while the growth after 2002 in CEDS driven by China (mainly coal) seems to be overestimated. Much lower posterior natural BIO and GEO emissions than bottom-up priors (Etiope & Schwietzke, 2019; Saunois et al., 2020) (Figures 6e and 6f) account for the overestimation in total CH_4 emissions (Figure 6a) and simulated atmospheric CH_4 (Figure 1a) in prior scenarios. Although our isotope-based approach cannot in principle differentiate anthropogenic from natural BIO sources and their trends over the industrial period, the overall overestimation of BIO sources cannot be attributed to anthropogenic BIO because it was present already in 1750, when anthropogenic BIO sources were small. Because GEO and BB CH_4 emissions are relatively small, there is no other way to match atmospheric CH_4 concentrations in 1750. The posterior OH anomaly, derived from the product of our posterior f_{loss} (Figure 2h) and prior OH anomaly taken from multimodel ESMs (Stevenson et al., 2020), shows a slightly weaker but increasing trend following the prior over 1980–2015 (Figure 6g).

Table 2
Summary of Averaged Posterior Global CH_4 Budget From Our Base Simulations and Previous Top-Down Estimates

	This study[a]		Saunois et al. (2020) [b]		Schwietzke et al. (2016)	Fujita et al. (2020)	Lassey, Lowe, and Smith (2007)	Hmiel et al. (2020)[c]
Period	1986–2000	2003–2012	2008–2017	2008–2017	2003–2013	2003–2012	1986–2000	2003–2013
Atmospheric constraints	CH_4, $\delta^{13}C$, δD, $\Delta^{14}C$		CH_4 (*Top-down*)	*None (bottom-up)*	CH_4, $\delta^{13}C$	CH_4, $\delta^{13}C$, δD	CH_4, $\Delta^{14}C$	CH_4, $\delta^{13}C$, $\Delta^{14}C$
Total emissions (Tg CH_4 yr^{-1})	536 [506, 564]	568 [532, 601]	576 ± 15	737 ± 98	593	558	560 ± 40	–
Total Biogenic emissions (Tg CH_4 yr^{-1})	384 [360, 409]	406 [379, 433]	427 ± 21	531 ± 44	355 ± 27	346	–	–
Biomass burning Emissions (Tg CH_4 yr^{-1})	37 [28, 45]	31 [21, 41]	30 ± 5	30 ± 5	43 ± 9	50	–	–
Anthropogenic fossil emissions (Tg CH_4 yr^{-1})	112 [93, 130]	128 [103, 152]	111 ± 17	128 ± 14	145 ± 23	162	168 ± 16	177 ± 37
Geologic emissions (Tg CH_4 yr^{-1})	3.4 [1.0, 6.7]		8 ± 3	45 ± 14	51 ± 20			1.6 [0, 5.4]
Total fossil fraction (%)	21 [18, 25]	23 [19, 27]	21 ± 3	24 ± 4	33 ± 5	29	30 ± 2	–

Note. Here CEDS, EDGARv5, and EDGARv6 scenario results are averaged. Uncertainties are reported as 68% CI (this study) or 1 SD, (previous studies), except for geologic emissions in Hmiel et al. (2020) reported as 95% CI. [a]Geologic emissions are presented for the average of 1850–2015 since they are assumed to be time-invariant. [b]All 1 SD values of Saunois et al. (2020), presented here, are roughly estimated from the minimum and maximum values of corresponding emission categories in Table 3 of Saunois et al. (2020). The "other natural sources" (37 Tg CH_4 yr^{-1}) of top-down estimates, presented in Saunois et al. (2020), is assigned to geologic emissions by 8 Tg CH_4 yr^{-1} (i.e., geological, permafrost soil, and hydrates) and natural biogenic emissions by 29 Tg CH_4 yr^{-1} (i.e., freshwater, wild animals, termites, and biogenic ocean) based on the proportion of bottom-up estimates for the same period. [c]Only preindustrial $\Delta^{14}C$-CH_4 and modern $\delta^{13}C$-CH_4 data are used.

Because the posterior results among CEDS, EDGARv5, and EDGARv6 scenarios are consistent, hereafter, we refer to the average of the three scenarios as our posterior global CH_4 budget.

We calculate decadal averages of each scenario for 2003–2012 and 1986–2000, and compare our results with recent GCP estimates (Saunois et al., 2020) and isotopic studies (Fujita et al., 2020; Hmiel et al., 2020; Schwietzke et al., 2016), as well as the most recent $\Delta^{14}C$-CH_4 study estimating global FF emissions from their $\Delta^{14}C$-CH_4 data (Lassey, Lowe et al., 2007) (Table 2). Our global total CH_4 emissions (~568 Tg CH_4 yr^{-1}) are similar to the top-down GCP estimates, as expected because our total CH_4 lifetime (~9 years), based on Prather et al. (2012), also resembles that in the GCP estimates. The BIO and BB emissions are also similar between ours and top-down GCP estimates, which are larger and smaller than those in stable isotope estimates, respectively.

To compare our results for anthropogenic FF emissions to previous studies, Figure 7 shows our average posterior anthropogenic FF emissions, together with previous bottom-up and top-down estimates. Our posterior anthropogenic FF emissions for 2003–2012 (128 [103, 152] Tg CH_4 yr^{-1}; mean and 68% CI, given by 16th and 84th percentiles) are lower than previous isotopic-based estimates and are not consistent with their negative or zero FF trends after 2007 (Fujita et al., 2020; Hmiel et al., 2020; Schwietzke et al., 2016). Between 2000–2006 and 2007–2013, our posterior estimates indicate an increase in anthropogenic FF emissions (14.2 [6.3, 22.3] Tg CH_4 yr^{-1}), an increase in total BIO emissions (16.1 [8.1, 24.1] Tg CH_4 yr^{-1}), a slight decrease of BB emissions (−5.0 [−8.4, −1.5] Tg CH_4 yr^{-1}), and a slight increase of the total CH_4 loss rate (1.5 [0.3, 2.7]%). However, the interpretation of recent CH_4 growth is complicated by poorly constrained global OH trends (see Section 3.3). A newer version of CEDS, prepared for CMIP7 experiments (O'Rourke et al., 2021), shows that the FF emission increase after 2002 was revised downward compared to the previous CEDS emissions, while the FF emissions in 1970s were strongly increased, which is similar to EDGARv5 but inconsistent with our results. The UNFCCC inventory for anthropogenic FF emissions, compiled as the Global Fuel Emissions Inventory version 2 (GFEIv2; Scarpelli et al., 2022), is much lower than the other estimates.

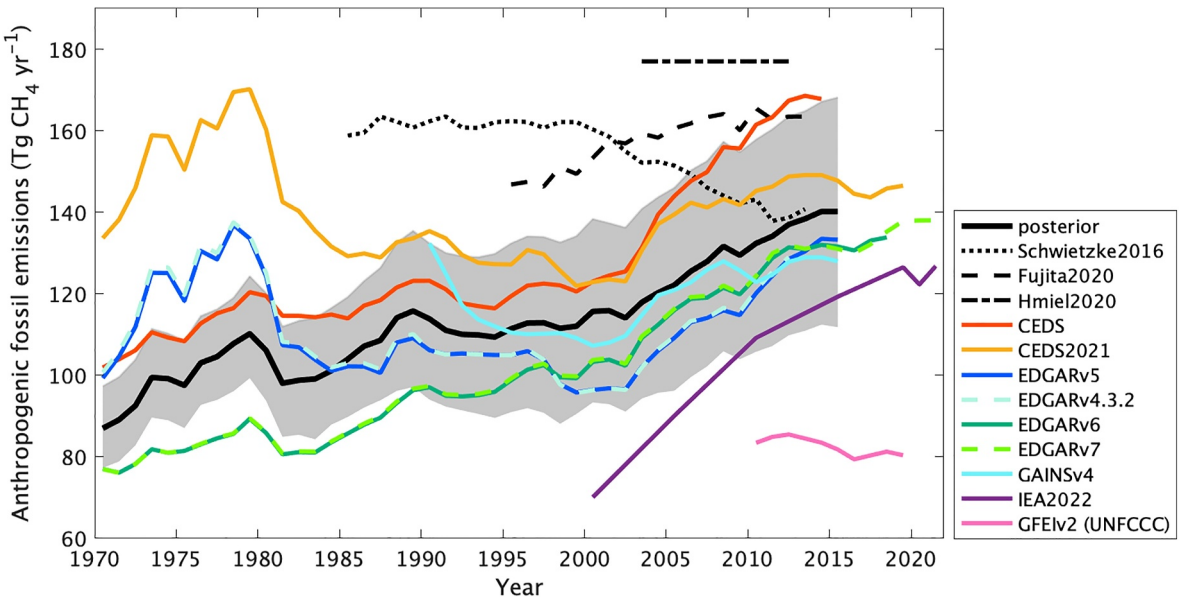

Figure 7. Time series of global anthropogenic fossil CH_4 emissions from 1970. Our posterior mean and 68% CI, derived from averages of CEDS, EDGARv5, and EDGARv6 scenarios, are presented by the solid black line and the gray band, respectively. The time series data for 1970–2015 are available in Dataset S2, including other source categories and parameters. The estimates in previous isotope-based top-down studies are presented by black lines: Schwietzke et al. (2016) (dotted line)[a], Fujita et al. (2020) (dash line)[b], and Hmiel et al. (2020) (chain line)[c]. Other colored lines show different anthropogenic fossil CH_4 emission inventories: CEDS version 2017-05-18 (red), EDGARv5 (blue), EDGARv6 (green), EDGARv4.3.2 (Janssens-Maenhout et al., 2019) (dashed cyan), EDGARv7 (Crippa et al., 2022) (dashed light green), CEDS version 2021-04-21 (O'Rourke et al., 2021) (orange), GAINSv4—IIASA's Greenhouse gas and Air pollution INteractions and Synergies (Höglund-Isaksson et al., 2020) (light blue)[d], IEA—International Energy Agency, Global Methane Tracker 2022 (IEA, 2022) (purple)[e], and Global Fuel Emissions Inventory version 2 (GFEIv2) (Scarpelli et al., 2022)[f] (pink). Note that EDGARv5 is derived from EDGARv4.3.2 and that EDGARv6 derives to EDGAR7 (i.e., these lines are overlapped in the figure, respectively). [a] Calculated from total fossil fuel (FF) emissions in Figure 2a of Schwietzke et al. (2016) minus geologic emissions in Table 1 of Schwietzke et al. (2016). [b] Taken from total FF emissions in Figure 9a of Fujita et al. (2020) because no geologic sources are used in their prior emission. [c] Taken from period averages for 2003–2012 in Hmiel et al. (2020)—total fossil emissions derived from modern atmospheric δ^{13}C-CH_4 data in Schaefer et al. (2016) minus geologic emissions derived from Hmiel et al. (2020)'s preindustrial atmospheric Δ^{14}C-CH_4 data. [d] Taken from Figure 6b of Höglund-Isaksson et al. (2020). [e] Only available in 2000, 2005, 2010, 2015, and 2019–2021 and the emission from the bioenergy sector is excluded. [f] Taken from Table 1 of Scarpelli et al. (2022) and Figure 3 of Shen et al. (2023).

3.2. Correlations in Global CH_4 Budget

Next, we explore the correlations between our posterior source emissions and parameters. Because we also optimize the total CH_4 loss rate, which is strongly correlated with posterior emission strength (Figure S2 in Supporting Information S1), we present correlations with source fractions—the proportion of global total CH_4 emissions as specific source CH_4 emissions (Figure 8). Here, global total BIO (anthropogenic plus natural BIO), global total FF source (anthropogenic FF plus GEO), and BB source fractions, averaged over 2003–2012, are presented. Similarly, we calculate total BIO and FF isotopic source signatures ($\delta^{13}C_{bio}$, $\delta^{13}C_{ff}$, δD_{bio}, and δD_{ff}) by emission-weighted means derived from natural and anthropogenic sources.

A high correlation ($|R| \geq 0.5$) is observed between all source fractions and ϕ (Figures 8ab, 8ac, and 8ad), and between total BIO fraction and $\delta^{13}C_{bio}$ and KIE^D (Figures 8d and 8y), indicating the importance of these parameters for estimating global sectorial source fractions under our model settings. Skewed distributions are observed in posterior KIE^C around the upper bound of our prior range, which could affect the correlation between sectorial source fractions. To extract the primary correlations in the global CH_4 budget shown in Figure 8, we focus on the relationships between BIO and FF fractions with $\delta^{13}C_{bio}$ and ϕ in Figure 9 and compare our results with those in previous studies.

For global total FF source fractions versus global total BIO source fractions averaged over 2003–2012 (Figure 9a), a strong negative correlation ($R = -0.90$) is found, as expected because these are the two major source fractions (>90%). Deviation from a straight line arises from differences in the BB fraction. Although our all posterior ensembles cover all estimates in previous studies presented here, we find our posterior mean FF fraction, 23.1 [19.0, 26.8] % (mean and 68% CI), is generally lower than those in stable isotope-based studies (28%–33%) (Basu et al., 2022; Fujita et al., 2020; Lan et al., 2021; Schwietzke et al., 2016; Thanwerdas et al., 2022) and more

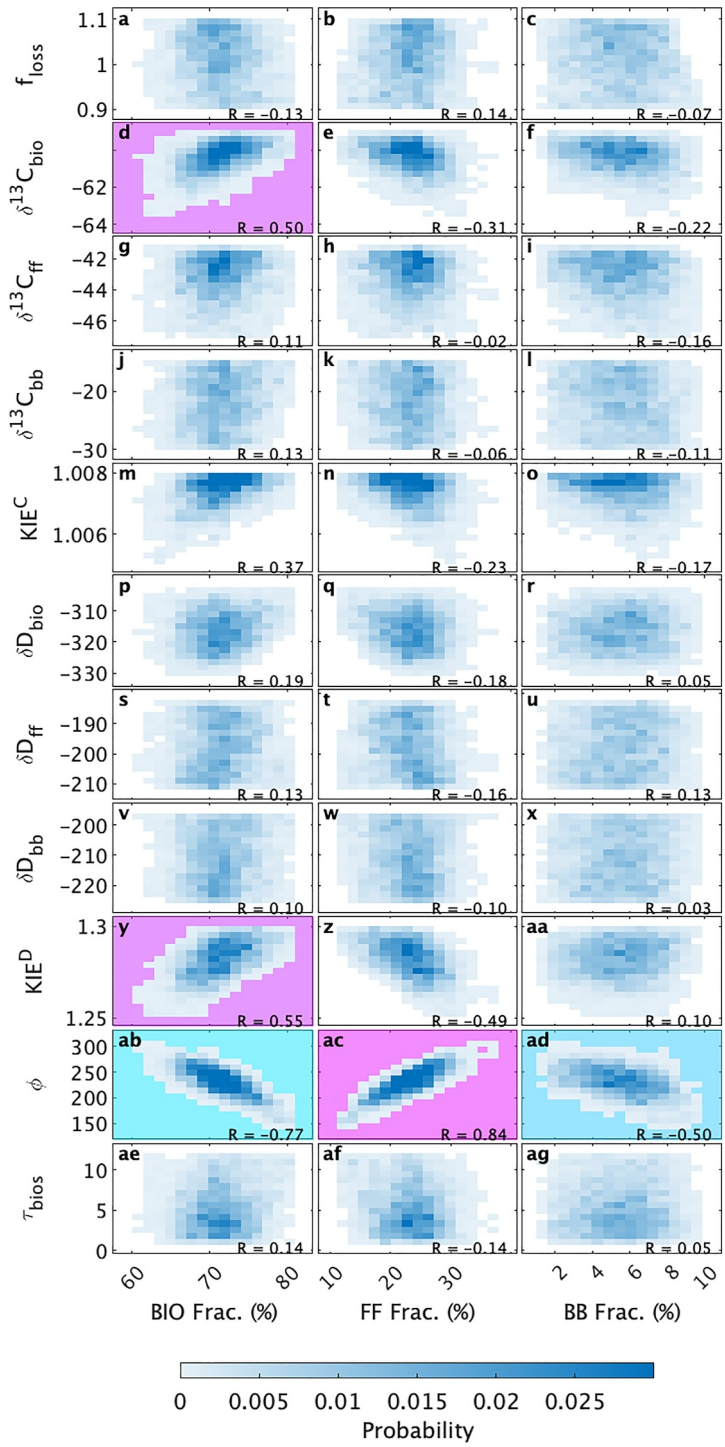

Figure 8. Two-dimensional histograms of our all posterior results in our base simulation (blue shades) for global total biogenic (BIO) fraction (left column), global total fossil fuel (FF) fraction (middle column), and global biomass burning (BB) fraction (right column) of emissions versus scaling factors of the total loss rate (f_{loss}) and all isotopic parameters (see Table 1) averaged over 2003–2012. Strong positive correlations ($R \geq 0.5$) are highlighted in pink and strong negative correlations ($R \leq -0.5$) in blue. Two-dimensional histograms for other combinations of emissions and parameters are presented in Figures S2–S4 in Supporting Information S1.

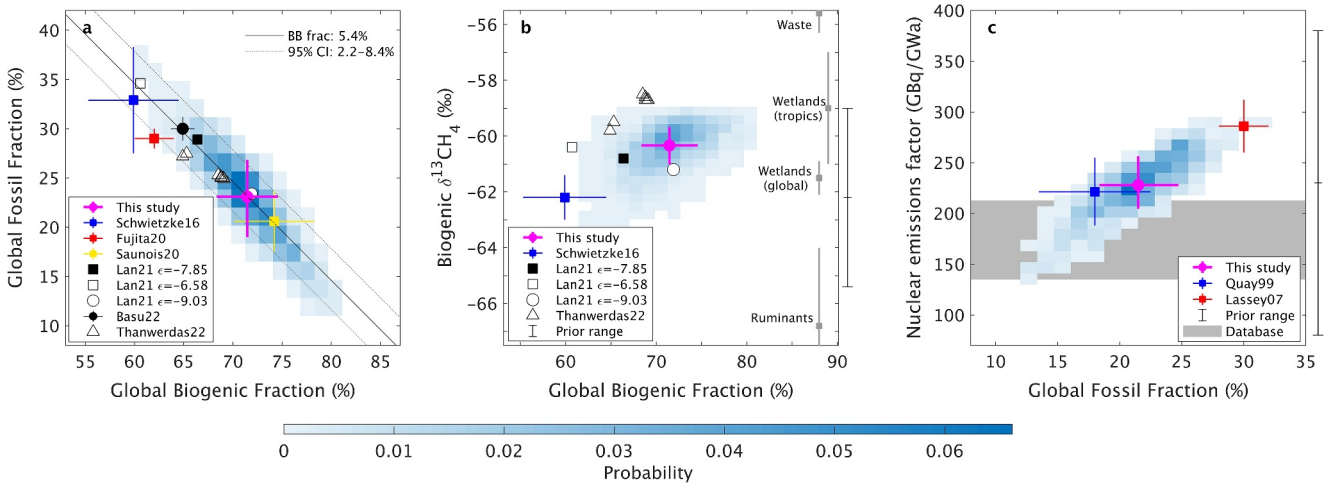

Figure 9. Two-dimensional histograms of all posterior results (blue shades) and overall average and 68% CI (pink) for global fossil source fraction versus global biogenic source fraction averaged over 2003–2012 (a), biogenic δ^{13}C-CH_4 source signature versus global biogenic source fraction averaged over 2003–2012 (b), and global NPP $^{14}CH_4$ emissions factor (ϕ) versus global fossil source fraction averaged over 1986–2000 (c). Black lines in (a) show the relationship under our posterior biomass burning fractions (posterior mean and 95% CI). Black bars outside the right axis in b and c show our full prior parameter ranges. Prior mean and full ranges of our global biogenic fraction and global fossil fractions are 72.3 [43.5–91.6] % and 23.6 [6.8–51.2] %, respectively (not shown). Gray bars in b show δ^{13}C-CH_4 signatures (±1 SD) from Schwietzke et al. (2016) for selected major biogenic sources, except for tropical wetlands from MOYA/ZWAMPS Team et al. (2022). Results of previous studies are also plotted (Basu et al., 2022; Fujita et al., 2020; Lan et al., 2021; Lassey, Lowe, & Smith, 2007; Quay et al., 1999; Saunois et al., 2020; Schwietzke et al., 2016; Thanwerdas et al., 2022) (Error bars represent 1 SD when available). The results in Quay et al. (1999) are period averages for 1990–1993, Lan et al. (2021) and Basu et al. (2022) for 1999–2016, and Thanwerdas et al. (2022) for 2014–2015, respectively. ϵ in (a) and (b) represents the fractionation factor, which equals to $(1/KIE^C - 1) \times 1{,}000$ (‰). Gray shades in c represents our updated data-based estimates of global NPP emission factor for 1986–2000 (95% CI) (see Section 2.5).

consistent with GCP estimates based on inversions with CH_4 mole fraction only (Saunois et al., 2020) (Figures 9a and Table 2).

Global total BIO source fraction averaged for 2003–2012 is strongly correlated with global total BIO δ^{13}C-CH_4 source signature (Figure 9b, same as Figure 8d). Higher BIO δ^{13}C-CH_4 source signatures correlate with higher global total BIO fractions to balance the atmospheric $^{13}CH_4$ budget, resulting in lower global total FF fraction than in the recent isotope-based estimates (Figure 9b and Table 2). We find our optimized total BIO δ^{13}C-CH_4 source signature, −60.2 [−61.0, −59.7] ‰, is about 2‰ higher than those in the database-derived estimates in Schwietzke et al. (2016) (Figure 9b). Their database estimate of mean BIO δ^{13}C-CH_4 source signature could potentially be biased, because of limited data availability in the tropics where BIO isotopic signatures are higher than those in the extratropics, and because of uncertainty in the proportions of latitudinal BIO emission strength (Schwietzke et al., 2016; Sherwood et al., 2017). Recent studies of δ^{13}C-CH_4 data have also used heavier total BIO δ^{13}C-CH_4 signatures and found higher BIO fractions than Schwietzke et al. (2016) (Basu et al., 2022; Lan et al., 2021; Thanwerdas et al., 2022). The choice of KIE^C also influences the relationship between BIO δ^{13}C-CH_4 and total BIO source fraction, where higher KIE^C is correlated with higher total BIO source fraction in the results of Lan et al. (2021) (Figure 9b). We also found a positive correlation between total BIO source fraction and KIE^C (Figure 8m), although the strength of the correlation was not as high as for BIO δ^{13}C-CH_4. Similar to our posterior ensemble results, Thanwerdas et al. (2022) also present clear negative correlations between BIO δ^{13}C-CH_4 source signature and BIO source fraction in their sensitivity test results on the assimilation setup of δ^{13}C-CH_4 source signatures (Figure 9b).

There is a clear positive correlation between the total FF source fraction and the global NPP $^{14}CH_4$ emissions factor ϕ due to their opposite effects on atmospheric Δ^{14}C-CH_4 (Figure 9c, same as Figure 8ac but for 1986–2000). Our estimated FF fraction (21.5 [18.3, 24.7]%) and ϕ (230 [205, 256] GBq/Gwa) are both lower than Lassey, Lowe et al., 2007 (30 ± 2.3% and 286 ± 26 GBq/GWa, mean ± 1 SD), but consistent with an earlier estimate (Quay et al., 1999). Despite large variability in ϕ observed at individual reactors, our updated observation-based estimate (Section 2.5) suggests the plausible range of the global mean ϕ is only 135–213 GBq/GWa (95% CI) for 1986–2000. This observation-based estimate is independent from but supports our lower posterior FF fraction (Figure 9c).

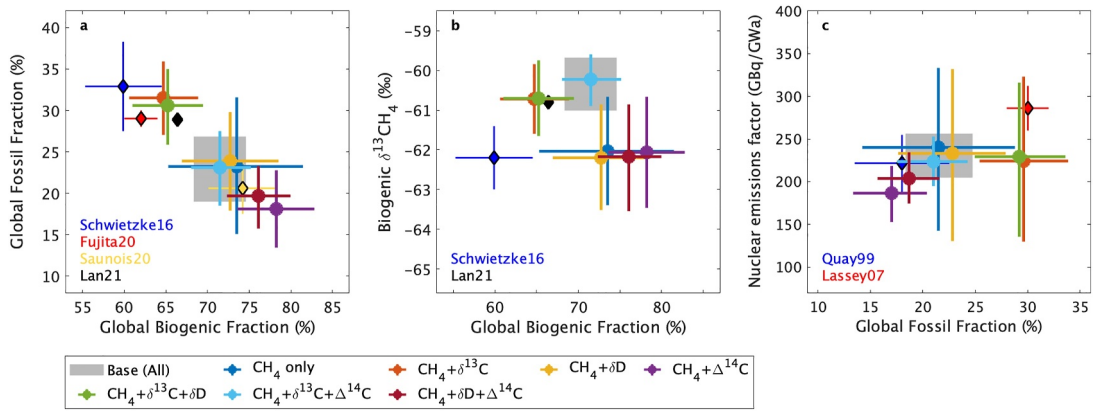

Figure 10. Same as Figure 9, but for overall average and 68% CI in the base simulation represented by gray shades (originally pink in Figure 9), and those in the sensitivity tests that applied different combinations of observational constraints to the simulation (colored circles with error bars, 68% CI). Other observational or parameter settings were kept the same as the base simulation. Results of selected previous studies (colored diamonds, mean and 1 SD) are also plotted, same as in Figure 9. The result "Lan21" (black diamonds) is taken from their default result under $\varepsilon = -7.85‰$ (the same as black squares in Figures 9a and 9b). Note that clear correlations are only seen among the scenarios in Figure 10b or Figure 10c when atmospheric δ^{13}C-CH_4 or Δ^{14}C-CH_4 are used as observational constraints, respectively (i.e., In other cases, posterior mean biogenic δ^{13}C-CH_4 signatures or NPP emission factors remain almost the same as their prior distributions).

3.3. Sensitivity Tests

To investigate the impact of different prior model settings on the estimated global source fractions, we performed multiple sensitivity tests under (a) different observational isotope constraints (Obs; e.g., CH_4 only, $CH_4+\delta^{13}C$, etc.) and (b) different prior ranges of selected parameters (ParaRange; i.e., changing the freedom of the parameters) (see Table S3 in Supporting Information S1). These tests are useful not only to investigate the impact of different model settings to our base simulation results but also to directly compare our results with previous studies by running our model with similar settings to theirs.

Figure 10 shows the correlation plots in the CH_4 budget among the tests, which is the same as Figure 9 but for overall average and 68% CI in each simulation under different observational isotopic constraints (also see Table 3 for the summary of these tests). The time series of posterior sectorial source fractions and simulated atmospheric isotopic histories under the different isotopic constraints are presented in Figures S5 and S6 in Supporting Information S1, respectively.

Comparing with CH_4-only inversion results, where the FF fraction for 2003–2012 is 23.2 [15.1, 31.6] % (Figure 10, blue circles), incorporating δ^{13}C-CH_4 constraints yields higher FF fractions (31.5 [27.0, 35.9] %, red circles). This "$CH_4+\delta^{13}C$" case is consistent with Schwietzke et al. (2016), where higher FF fractions than "CH_4-only" inversion are obtained under additional δ^{13}C-CH_4 constraints. This confirms that our model setup and approach does result in higher FF fractions when only δ^{13}C-CH_4 constraints are applied, which is similar to previous δ^{13}C-CH_4 based estimates (e.g., Basu et al., 2022; Lan et al., 2021; Schwietzke et al., 2016).

For a case with "$CH_4+\Delta^{14}C$", lower FF fractions (18.1 [13.5, 22.7] %, purple circles) are found, in comparison to the "CH_4-only" case. This result is contrary to Lassey, Etheridge, et al. (2007), where higher FF fractions of 30 ± 2% were derived from Δ^{14}C-CH_4 data for 1986–2000 (Figure 10c and Table 2). The difference appears to arise from the methods used by Lassey, Etheridge, et al. (2007), who applied a regression approach rather than an explicit model. This is discussed further in Section 4.

Table 3
Summary of Our Posterior Global Total Fossil Fuel Fractions for 2003–2012 Derived From Different Observational Constraints, as Presented in Figure 10

	Prior	CH_4 only	$CH_4+\delta^{13}C$	$CH_4+\delta D$	$CH_4+\Delta^{14}C$	Base (all)
Fossil fraction (%)	23.6 [17.2, 30.1]	23.2 [15.1, 31.6]	31.5 [27.0, 35.9]	23.9 [17.9, 29.8]	18.1 [13.5, 22.7]	23.1 [19.0, 26.8]
Error reduction ratio	–	−28%	31%	8%	29%	40%

Note. Uncertainties are reported as 68% CI. The error reduction ratio is defined as $-(\sigma^{pos}-\sigma^{pri})/\sigma^{pri} \times 100\%$, where σ^{pos} and σ^{pri} are posterior and prior uncertainties, respectively. Result under a different prior scenario excluding freshwater emissions (NoFRESHem) is also presented in Table S5 of the Supporting Information S1.

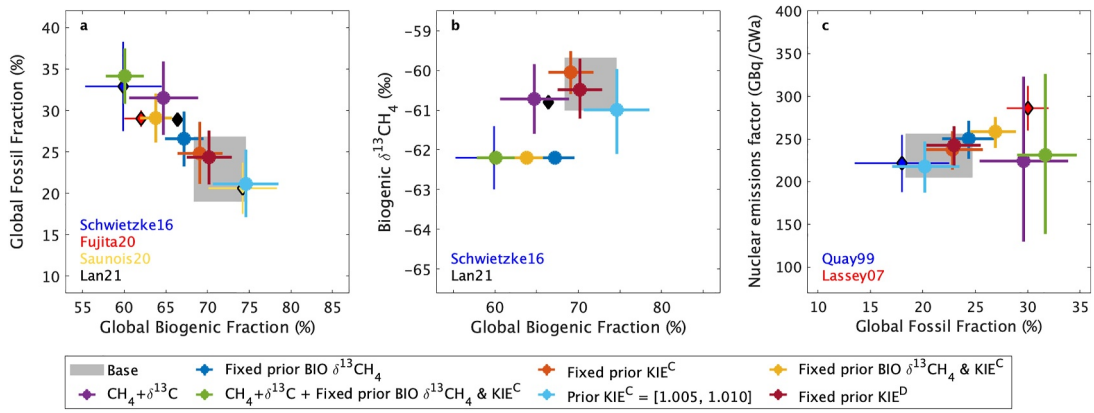

Figure 11. Same as Figure 10, but for sensitivity tests that applied different prior mean biogenic δ^{13}C-CH_4 source signatures, KIE^C, and KIE^D. "$CH_4+\delta^{13}C$" is the same as in Figure 10.

The mean FF fraction with the inclusion of δD-CH_4 (23.9 [17.9, 29.8] %, yellow circles) is barely changed from the "CH_4-only" case, although the uncertainty is reduced. Such limited contributions of δD-CH_4 to the mean sectorial fraction attribution is also seen in Fujita et al. (2020), who utilized both δ^{13}C-CH_4 and δD-CH_4 data and found sectorial source fractions similar to Schwietzke et al. (2016) (Figure 10a and Table 2). The potential explanation of weak constraints by δD-CH_4 is addressed in Section 4.

With all isotopic constraints, our base simulation eventually yields a similar posterior mean FF fraction to the prior estimate and "CH_4-only" results, but the uncertainty range is significantly reduced by 40% and 53% relative to their estimates, respectively, as 23.1 [19.0, 26.8] % (Figure 10, gray shades) (also see Table 3). It should be noted that the similarity between our posterior FF fraction under all isotopic constraints and those in top-down CH_4 inversions (e.g., Saunois et al., 2020) is not an accident of our model setup, but rather the result of simultaneous constraints by atmospheric δ^{13}C-CH_4 and Δ^{14}C-CH_4 (Figure 10 "CH_4 + δ^{13}C + Δ^{14}C", light blue). Note that the uncertainty range in our CH_4-only results is larger by 28% than that in the prior estimate due to the inconsistent posterior solutions among the CEDS, EDGARv5, and v6 scenarios (Figure S7 in Supporting Information S1).

Figure 11 shows the sensitivity test results that applied different prior settings of BIO δ^{13}C-CH_4 source signatures, KIE^C and KIE^D (ParaRange #1–6; Table S3 in Supporting Information S1). Fixing the prior BIO δ^{13}C-CH_4 source signature as its prior mean (−62.2‰) yields higher FF fractions (26.6 [23.2, 29.8]) (Figure 11, blue circle), as does fixing KIE^C at its prior mean (1.0065) (24.8 [21.1, 28.6], red circle). Further increases in FF fraction are obtained when both parameters are fixed (29.1 [26.1, 32.0], yellow circle) and even more under "$CH_4+\delta^{13}C$" (34.1 [30.8, 37.5], green circle), resembling the model settings and results in Schwietzke et al. (2016). Expanding the prior KIE^C range to [1.005, 1.010], considering potential maximum tropospheric Cl contributions (Table S4 in Supporting Information S1), yields lower FF fractions, 21.1 [17.1, 25.2] (light blue circle), though within the uncertainty of those from our base result. The posterior mean KIE^C obtained from this test (1.0091 [1.0084, 1.0097]) surpasses our posterior base result (1.0075 [1.0070, 1.0078]), indicating the upper limit we used on KIE^C constrained the posterior result. Fixing the prior mean KIE^D (1.275) does not lead to a significant change in the posterior mean in FF fraction but reduces the uncertainty from the base result (brown circle).

Figure 12 shows the results that applied different prior ϕ settings (ParaRange #8–13; or Table S3 in Supporting Information S1). We find our posterior results, both in base simulation or "$CH_4+\Delta^{14}C$", do not change even when our prior ϕ is replaced by Lassey et al.'s mean estimate (286 [136, 436] GBq/GWa; the min.–max. range is the same as our base setting) or even replaced by much wider prior range (300 [0, 600] GBq/GWa) (Figure 12, blue, red, and green circles). This indicates our posterior ϕ is well constrained by atmospheric Δ^{14}C-CH_4 data. When the prior ϕ is fixed at 286 GBq/GWa, however, higher mean FF fractions (~27%) are obtained for 1986–2000 as seen in Lassey, Lowe, et al. (2007), both in base simulation or "$CH_4+\Delta^{14}C$" (yellow and light blue circles). We also find the sensitivity is not significant when fixing the prior mean τ_{bios} (brown circle).

The sensitivity of the prior BB emissions are also investigated by allocating "RCO" emissions (Section 2.1) from prior FF to prior BB emissions, in addition to the BB4CMIP (RCOem; Table S3 in Supporting Information S1),

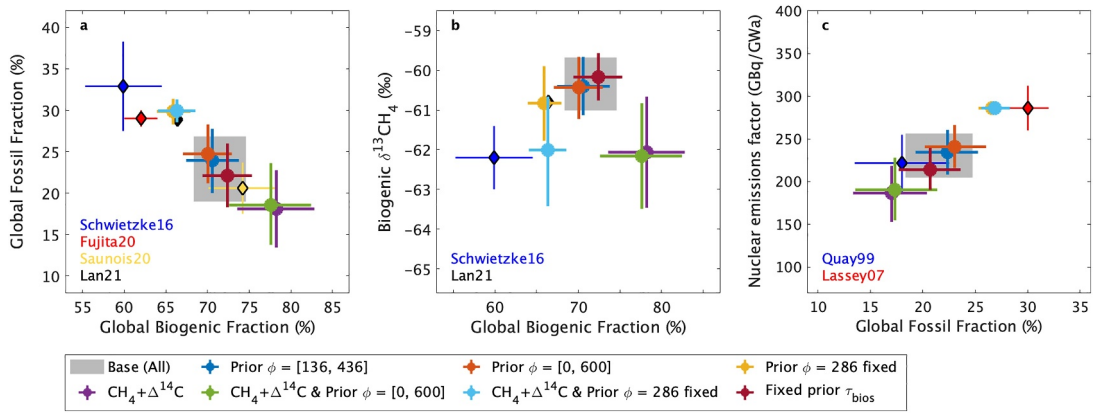

Figure 12. Same as Figure 10, but for sensitivity tests that applied different prior NPP emission factors (ϕ) and biospheric turnover time (τ_{bios}). "CH_4+$\Delta^{14}C$" is the same as in Figure 10.

showing slight lower posterior FF fractions, 21.0 [16.7, 25.2] % (and higher BB fractions), though within the uncertainty of our base result (Figure S8 in Supporting Information S1). In this regard, our sensitivity test under a narrower prior f_{bb} range ([0.5, 1.5]) (ParaRange #14; Table S3 in Supporting Information S1) shows slightly higher FF fractions of 25.3 [22.3, 28.4] % for 2003–2012 than our base simulation to compensate the posterior lower BB fractions, despite also within the uncertainty of our base result (Figure S8 in Supporting Information S1). Applying the default f_{bb} range ([0.5, 3.5]) to other source scaling factors, f_{anth_bio}, f_{natr_bio}, and f_{anth_ff} (ParaRange #15), also does not change the mean posterior results (Figure S8 in Supporting Information S1).

To investigate the impact of different prior OH and wetland emission trends, four alternative prior OH scenarios and three alternative prior wetland scenarios are considered (OHtrend and IAWetBIOem; Table S3 in Supporting Information S1). The results indicate different OH and wetland trend scenarios do not change the mean FF fractions for 2003–2012 (Figure S9 in Supporting Information S1), but the different OH trends change the attribution of the cause of the recent CH_4 trend (Figure S10 in Supporting Information S1) and different wetland emission trends change the attribution of anthropogenic and natural BIO emissions (Text S1 in Supporting Information S1). Excluding prior freshwater emissions (NoFRESHem; Table S3 in Supporting Information S1) also does not change the mean FF fractions under all isotopic constraints ("Base") and "CH_4+$\Delta^{14}C$" case, but significantly changes the posterior results without constraints of $\Delta^{14}C$-CH_4 (e.g., "CH_4 only"; see Text S1, Figure S11, and Table S5 in Supporting Information S1), highlighting the merit of multi-isotopic constraints including $\Delta^{14}C$-CH_4 to robustly estimate the global CH_4 budget.

Applying upper bounds of potential $\Delta^{14}C$-CH_4, $\delta^{13}C$-CH_4 and δD-CH_4 interlaboratory differences (ObsIsoILD; Table S3 in Supporting Information S1) does not significantly change mean FF fractions, although the impact of δD-CH_4 interlaboratory differences could be the most influential (Figure S12 and Text S1 in Supporting Information S1). More careful consideration is also required if assimilating historical raw $\delta^{13}C$-CH_4 and δD-CH_4 data directly, whose uncertainty of interlaboratory differences is more significant than those in modern air samples (Umezawa et al., 2018).

4. Discussion

Several previous studies have utilized atmospheric $\delta^{13}C$-CH_4 as constraints for source partitioning (Basu et al., 2022; Hein et al., 1997; Lan et al., 2021; Schaefer et al., 2016; Schwietzke et al., 2016; Thanwerdas et al., 2022), and a few studies have further used δD-CH_4 (Fujita et al., 2020; Rice et al., 2016) or $\Delta^{14}C$-CH_4 (Hmiel et al., 2020; Lassey, Etheridge, et al., 2007; Quay et al., 1999), but no study synthesized all these constraints. This study is the first to utilize modern $\Delta^{14}C$-CH_4 data with available $\delta^{13}C$-CH_4 and δD-CH_4 data sets to estimate the global CH_4 budget and isotopic source signatures, KIEs, τ_{bios}, and ϕ over the industrial period.

Our posterior global CH_4 budget is fairly consistent with atmospheric CH_4-only top-down estimates from the GCP (Saunois et al., 2020), but not with recent stable isotope-based estimates (Basu et al., 2022; Fujita et al., 2020; Lan et al., 2021; Schwietzke et al., 2016) (Figure 9a and Table 2). In this study, we optimized

δ^{13}C-CH_4 and δD-CH_4 source signatures through our PF approach, considering plausible wide uncertainties of δ^{13}C-CH_4 and δD-CH_4 source signatures from the database (Schwietzke et al., 2016; Sherwood et al., 2017) (Table 1). We found that our optimized total mean BIO δ^{13}C-CH_4 source signature (−60.2 [−61.0, −59.7] ‰) is about 2‰ heavier than those in the prior database-driven estimate (Schwietzke et al., 2016), whereas our total mean FF δ^{13}C-CH_4 source signature (−43.1 [−44.3, −41.9] ‰) is not significantly changed from the database estimate. Recent findings show much larger tropical wetland emissions from African and Amazonian regions (France et al., 2022; Pandey et al., 2021; Shaw et al., 2022) than previous estimates, whose δ^{13}C-CH_4 source signatures are heavier than at higher latitudes, −60 to −55 ‰ (e.g., MOYA/ZWAMPS Team et al., 2022). Heavier tropical ruminant δ^{13}C-CH_4 source signatures (−60 to −50‰) have also recently been reported (Lu et al., 2021; MOYA/ZWAMPS Team et al., 2022). In this regard, Lan et al., 2021 presented heavier BIO δ^{13}C-CH_4 signatures than Schwietzke et al. (2016), utilizing the wetland δ^{13}C-CH_4 signature map from Ganesan et al. (2018), which considers spatial δ^{13}C-CH_4 differences. To validate such modeled isotopic signatures maps and the heavier global average BIO δ^{13}C-CH_4 signatures, more direct observations are required especially in the tropics.

Sink fractions approximately derived from our posterior total KIE^C and KIE^D are generally consistent with multiple-process model estimates (Saunois et al., 2020), indicating a tropospheric Cl contribution of ∼3% (∼18 Tg/yr under the total loss of 556 Tg/yr for 2003–2012) (Text S1 in Supporting Information S1). Our findings suggest the minimum tropospheric Cl scenario (∼1 Tg/yr) suggested by Gromov et al. (2018) is unlikely. Actually, when using a wider prior KIE^C range [1.005, 1.010] (ParaRange #5), we obtained even higher posterior total KIE^C (1.0091 [1.0084, 1.0097] vs. 1.0075 [1.0070, 1.0078]) and KIE^D (1.287 [1.279, 1.295] vs. 1.283 [1.274, 1.292]). While this suggests even higher tropospheric Cl contribution (van Herpen et al., 2023), the total KIE^C also aligns with a scenario presented in Lan et al. (2021) ($\varepsilon = -9.03$‰, open circles in Figures 9a and 9b), where the Cl contribution is 13 Tg/yr and the KIE^C of OH (KIE^C_{OH}) is higher, 1.0054 (Cantrell et al., 1990). Overall, top-down approaches can be affected by errors in KIE^C and δ^{13}C-CH_4, so improved constraints on KIE^C as well as δ^{13}C-CH_4 signatures would help to constrain the CH_4 budget. Recent studies disagree over whether current uncertainties in KIE^C or δ^{13}C-CH_4 signatures are more important (Basu et al., 2022; Thanwerdas et al., 2022). While our study is limited to a one-box model with global mean values, we believe that the large range of values we were able to consider may give a more comprehensive picture of the effect of these uncertainties than 3D model studies that are limited to a small number of sensitivity tests (see Text S1 in Supporting Information S1 for more details).

Our posterior FF fraction and ϕ, averaged for 1986–2000 (21.5 [18.3, 24.7]% and 230 [205, 256] GBq/GWa), are lower than those in Lassey, Lowe, et al. (2007) (30 ± 2.3% and 286 ± 26 GBq/GWa), despite our observational target encompassing their Δ^{14}C-CH_4 data (Figure S1 in Supporting Information S1). To check consistency with Lassey, Lowe, et al. (2007)'s method ("L07 method"), which used a linear regression approach to solve the mass balance equations of atmospheric Δ^{14}C-CH_4 and simultaneously derive total FF fraction and ϕ, we applied the L07 method to our Δ^{14}C-CH_4 data set over every possible 10-year or 15-year window over 1970–2008, assuming that our posterior FF fraction and ϕ were the only unknowns. We found the FF fractions estimated by the L07 method vary strongly depending on the analysis period, 15.5%–34.2% for FF fraction and 159–301 GBq/GWa for ϕ (Figure S13 in Supporting Information S1). Such large variations in FF fraction are not realistic and not consistent with our independent observation-based estimate of ϕ, implying that (a) there are numerous combinations of FF fraction and ϕ that align with atmospheric Δ^{14}C-CH_4 and (b) Lassey, Lowe, et al., 2007's estimate is not necessarily the optimal one but quite sensitive to the selected data period. Our posterior ensembles encompass Lassey, Lowe, et al., 2007's estimate, but the cumulative probability is less than 1% (see Figure 9c). Earlier Δ^{14}C-CH_4 studies (Manning et al., 1990; Quay et al., 1999; Wahlen et al., 1989), based on a basic box model analysis, estimated lower FF fractions of 16%–24% (Figure 9c), which are consistent with our results. Our lower FF fractions are also supported by our updated independent estimate from observed $^{14}CH_4$ emissions (Figure 9c). Further validation of NPP $^{14}CH_4$ emissions would enable for more robust FF emission estimates, particularly if utilizing a 3D model that requires spatiotemporally accurate prior emission data for each reactor.

Our posterior GEO emissions average 3.4 Tg CH_4 yr^{-1}, and are less than 8.8 Tg CH_4 yr^{-1} (97.5th percentile), which are much smaller than bottom-up estimates (Etiope & Schwietzke, 2019; Saunois et al., 2020; Schwietzke et al., 2016), but quite consistent with Hmiel et al. (2020). This is not surprising because we use the same ice core Δ^{14}C-CH_4 data with Hmiel et al. (2020) for the preindustrial era (but with a wider target range; see Table S1 in Supporting Information S1). In contrast, our modern posterior FF emissions are smaller than in Hmiel

et al. (2020), who used δ^{13}C-CH_4 observations for 1988–2013 in Schaefer et al. (2016), not their own Δ^{14}C-CH_4 data. Whereas Hmiel et al. (2020) reallocated CH_4 emissions from GEO to anthropogenic FF sources to close the budget, our analysis reallocates CH_4 emissions from GEO to total BIO sources (Figure 9a and Table 2). Importantly, our posterior emission scenario matches atmospheric δ^{13}C-CH_4 and δD-CH_4 histories, suggesting that smaller GEO and anthropogenic FF emissions are consistent with all isotopic data. In this regard, anthropogenic FF emission estimates of ∼130 Tg/yr reported by Lan et al. (2021) and Basu et al. (2022), consistent to ours, are strongly based on the prescribed GEO emissions of ∼37 Tg/yr, taken from Etiope et al. (2019). Thus, their anthropogenic FF emissions must increase to 150–170 Tg/yr, if GEO emissions are reduced.

Our finding that average anthropogenic FF emissions for 2003–2012 are similar to bottom-up estimates may appear to conflict with recent studies showing underestimated fugitive CH_4 emissions from oil and gas production regions (Alvarez et al., 2018), flaring sites (Plant et al., 2022), some urban regions (Sargent et al., 2021), and some unexpected CH_4 "superemitters" (Lauvaux et al., 2022). To reconcile these findings, it could be that underestimated fugitive emissions are not globally significant (given our uncertainty of 24 Tg CH_4 yr^{-1}, defined as the difference between the 84th percentile and mean), as suggested by a recent high-resolution inversion study (Shen et al., 2023), or that some other FF sources are overestimated in bottom-up inventories. Several atmospheric CH_4 inverse modeling studies (Saunois et al., 2020) have suggested that coal CH_4 emissions in China are overestimated in EDGARv4.2 and even in EDGARv4.3.2 despite the revision of coal emission factors (Maasakkers et al., 2019). Note that the fugitive CH_4 emission estimates in CEDS are based on EDGARv4.2 (Hoesly et al., 2018), that EDGARv5.0 is based on EDGARv4.3.2 (Crippa et al., 2020) (also see Figure 7), and that coal CH_4 emissions in China in EDGARv6 are even higher than those in EDGARv5.0, so the findings apply to our three prior emissions (Text S1 in Supporting Information S1). Such overestimation of coal emissions in China (or other biases) may therefore compensate underestimation of other FF sources.

We find higher BB fractions are required to increase both atmospheric δ^{13}C-CH_4 and Δ^{14}C-CH_4 levels (Figures S5 and S6 in Supporting Information S1), similar to Hein et al. (1997), who used the FF emission estimates based on Δ^{14}C-CH_4 (Manning et al., 1990; Wahlen et al., 1989) and then optimized other sources based on atmospheric δ^{13}C-CH_4. Our posterior BB emissions during 1750–1850 are 28 [22, 34] Tg/yr, which are 2.5 [1.9, 3.0] times as high as the BB4CMIP product used as our prior (van Marle et al., 2017). This suggests potential underestimation in BB4CMIP, where small fires (e.g., residential heating) may not have been detected well by satellites. Since van Marle et al., 2017 reported their products include agricultural waste burning, we did not include the BB emissions of CEDS and EDGAR scenarios in the prior, but we instead used a wider prior f_{bb} range in the base simulation to encompass the potential upper bounds of BB emissions reported in top-down estimates. More robust estimates of prior BB emissions would enable better constraints on BB emissions and the global CH_4 and isotopic CH_4 budgets.

We expected that assimilating δD-CH_4 data can strongly constrain the atmospheric sink due to larger KIE^D than KIE^C. However, our sensitivity tests showed that whether or not δD-CH_4 data were included, the posterior f_{loss} was not changed significantly. This is likely because (a) our prior base scenario with the tropospheric OH anomaly derived from ESMs (Stevenson et al., 2020) has already reproduced the values and trends in our atmospheric δD-CH_4 target over 1750–2015 (Figure 1c) and (b) our prior ranges of respective δD-CH_4 source signatures (±15‰) and KIE^D (1.25–1.30) were widely specified so that there are many combinations of parameters that can adjust the slight mismatch between observed and simulated atmospheric δD-CH_4. It is noted that our prior time-invariant OH scenario (OHtrend #1) did not well reproduce the rapidly increasing atmospheric δD-CH_4 trend after 1980, potentially supporting the increasing OH scenario for the period. To further constrain the atmospheric sink using atmospheric δD-CH_4 data, it is important to more robustly estimate prior δD-CH_4 source signatures and KIE^D, as well as to strengthen the observational constraint with more observations with inter-laboratory differences reduced.

Our posterior FF emissions remain an upward trend after 2002, which contradicts major stable isotope-based findings that suggest stable FF emissions and a significant rise in BIO emissions to explain atmospheric CH_4 growth and δ^{13}C-CH_4 decline after 2007 (Figures 1 and 7) (Basu et al., 2022; Fujita et al., 2020; Lan et al., 2021; Schwietzke et al., 2016). In contrast, Worden et al. (2017) suggested from their δ^{13}C-CH_4 box model analysis and satellite-based CO measurements that a decrease of BB emissions can reconcile simultaneous increase of FF and BIO emission after 2007, similar to our posterior results. Our sensitivity tests on different prior OH trends do not change the mean source fractions for 2003–2012 (Figure S9 in Supporting Information S1), but do change the

attribution of the cause of recent CH_4 trend (Figure S10 in Supporting Information S1). It is noted, however, because our model setups do not explicitly separate the different sink fractionations among tropospheric OH and other sinks (e.g., soil oxidations, stratospheric destructions), the decreasing OH scenarios here just need to be viewed as decreases of the total CH_4 loss rate. Thus, our sensitivity test results under decreasing OH scenarios did not reproduce the result presented in Lan et al. (2021), where different CH_4 loss processes are explicitly considered on their $\delta^{13}C$-CH_4 modeling. Different prior time-variable BIO $\delta^{13}C$-CH_4 signatures and KIE^C scenarios, as reported recently (e.g., Chang et al., 2019; van Herpen et al., 2023), could also impact the posterior trends. Further studies are needed to estimate robust prior trends in OH, isotopic source signatures, and KIEs, as well as to explicitly separate the OH and other sink fractionations in the optimization framework.

We think our simple one-box model approach using a PF has advantages compared to previous isotopic inversion studies by the (a) use of more isotopic tracers (δD-CH_4 and $\Delta^{14}C$-CH_4), (b) use of not only modern but also ice core and firn isotopic data, and (c) more comprehensive consideration of uncertainties in isotopic parameters (i.e., source signatures, KIEs, ϕ, and τ_{bios}), and (d) comprehensive sensitivity tests for each observational isotopic constraints and prior settings. This approach allowed us to optimize 20 parameters with large ensembles of simulations and to perform many sensitivity tests. However, we acknowledge there are limitations related to our simplized box model approach.

First, our one-box model cannot consider the spatial information on atmospheric tracers, prior sources and sinks, and atmospheric transport. It is well known there exists an interhemispheric difference and vertical gradient (e.g., troposphere to stratosphere) in atmospheric CH_4 and isotopes because of the heterogeneous CH_4 source and sink distributions and atmospheric transport. The neglect of such information can weaken actual observational constraints and limit our analysis and discussion (Naus et al., 2019). In this regard, our purpose of this study is to derive decadal-scale global mean CH_4 budget by synthesizing all available isotopic data since the preindustrial era, particularly using recently published ice core and firn $\Delta^{14}C$-CH_4 data from 1755 to 2013 (Hmiel et al., 2020), whose spatiotemporal density is very sparse. For a 3D model, assimilating the multiple tracers for mutidecadal time scale is still challenging due to the computation cost, complexity of model setup, and potential overfitting to limited data. We thus judged a simple global one-box model is the most reasonable and practical tool for the purpose of this study. Another challenge of our box model approach is estimating the global mean and uncertainty of isotopic observations under such sparse data coverage. In this study, we often utilized the Arctic and Antarctic data as the boundary values of the global mean, which could have overestimated the uncertainty. More atmospheric isotopic data, especially $\Delta^{14}C$-CH_4, will contribute to characterizing global means more robustly and refine the constraints provided.

Second, our posterior results still have large uncertainties on the estimated emission strengths and source and sink parameters, especially in their trends. This is primarily due to the high degree of freedom in our box model analysis and conservative choices for parameter ranges and observational target ranges (e.g., weak constraints on f_{loss} by atmospheric δD-CH_4, potentially due to the high degree of freedom in δD-CH_4 source signatures and KIE^D). Nonetheless, our historical atmospheric targets (even with decadal time-window) succeeded in narrowing down the initial parameter ranges before 1970, particularly for natural sources (i.e., E_{geo}, f_{natr_bio}, and their isotopic source signatures), as well as after 1970 for decadal mean global CH_4 budgets.

Finally, we acknowledge that multi-isotopic inversions using 3D transport models are promising when the isotopic data are globally available. In this regard, $\delta^{13}C$-CH_4 inverse modeling is recently being attempted (Basu et al., 2022; Thanwerdas et al., 2022), where uncertainty in tropospheric Cl contributions and KIE^C of OH, as well as BIO $\delta^{13}C$-CH_4 source signatures are important. It is still challenging to perform δD-CH_4 inverse modeling due to spatially sparse atmospheric data and large uncertainties in δD-CH_4 source signatures and KIE^D, but further detailed analysis of spatiotemporal variability in atmospheric δD-CH_4, in addition to $\delta^{13}C$-CH_4, could provide an important constraint on CH_4 sources and sinks (e.g., Warwick et al., 2016). Additional observational constraints of CH_3CCl_3 or other OH tracers (e.g., Rigby et al., 2017) would also be promising to constrain OH strengths and trends, although this also requires additional tracer parameters to be implemented and potentially optimized. For $\Delta^{14}C$-CH_4, new development of CH_4 sampling techniques has the potential to increase the number of $\Delta^{14}C$-CH_4 data (Zazzeri et al., 2021, 2023). Baseline clean data, urban polluted data, and downwind data from PWR nuclear facilities are all valuable to better constrain CH_4 sources and NPP emissions.

5. Conclusions

This study is the first to resolve the global CH_4 budget that is consistent with long-term atmospheric CH_4, $\delta^{13}C$-CH_4, δD-CH_4, and $\Delta^{14}C$-CH_4 data for 1750–2015. Our posterior anthropogenic FF CH_4 emissions are about 130 Tg CH_4 yr^{-1} for 2003–2012, which is higher than those reported by national governments to the UNFCCC but supports recent GCP estimates (Saunois et al., 2020). Critically, our multi-isotopic analysis does not support recent claims of underestimated global anthropogenic FF CH_4 emissions, which rely on limited isotopic data (Hmiel et al., 2020; Schwietzke et al., 2016). We find modern atmospheric $\Delta^{14}C$-CH_4 data rather constrain lower global FF source fractions, which is contrary to previous finding by Lassey, Etheridge et al., 2007, and Lassey, Lowe et al., 2007, but supported by an independent estimate of global nuclear $^{14}CH_4$ emissions. We show that multi-isotopic observational constraints can reduce the uncertainty of the global CH_4 budget, which is essential for effective CH_4 emission mitigation under the Global Methane Pledge.

Data Availability Statement

The observational target data of atmospheric CH_4, $\delta^{13}C$-CH_4, δD-CH_4, and $\Delta^{14}C$-CH_4 (available in Table S1 in Supporting Information S1) are constructed from the original data in these studies (Dlugokencky et al., 2021; Ferretti et al., 2005; Fujita et al., 2020; Hmiel et al., 2020; Lassey, Etheridge, et al., 2007; Mischler et al., 2009; Meinshausen et al., 2017; Michel et al., 2021; Rice et al., 2016; Schaefer et al., 2016; Schwietzke et al., 2016; White et al., 2016). The model data that support the major findings of this study are available from Dataset S1 and Dataset S2. The model code for the atmospheric box model with particle filter coded in MATLAB is available at https://github.com/ryo-fujita/BoxCH4model2024, or at the permanent Zenodo version here: doi: 10.5281/zenodo.14614127.

Acknowledgments

We sincerely thank E. Dlugokencky at NOAA/GML for the atmospheric CH_4 data; A. Rice at Portland State University; B. H. Vaughn at INSTAAR; T. Umezawa at Tohoku University (now at National Institute for Environmental Studies); J. Mischler at Pennsylvania State University (now at Goshen College) for the atmospheric $\delta^{13}C$-CH_4 and δD-CH_4 data; and H. Schaefer, K. Lassey, and G. Brailsford at NIWA for the atmospheric $\delta^{13}C$-CH_4 and $\Delta^{14}C$-CH_4 data. We also thank Dr. Sourish Basu and two anonymous reviewers for their helpful comments and suggestions. We are grateful to X. Lan at NOAA/GML, S. Schwietzke at Environmental Defense Fund, and K. Kawamura at National Institute of Polar Research for constructive comments on the initial manuscript. European Research Council (ERC) under the European Union's Horizon 2020 research and innovation program (Grant agreement 679103). Ministry of Education, Culture, Sports, Science and Technology (MEXT), Japan, through the JSPS KAKENHI (21K17883 and 24K00702) and through Arctic Challenge for Sustainability II (ArCS II) Project (JPMXD1420318865).

References

Alvarez, R. A., Zavala-Araiza, D., Lyon, D. R., Allen, D. T., Barkley, Z. R., Brandt, A. R., et al. (2018). Assessment of methane emissions from the U.S. oil and gas supply chain. *Science*, *361*(6398), 186–188. https://doi.org/10.1126/science.aar7204

Basu, S., Lan, X., Dlugokencky, E., Michel, S., Schwietzke, S., Miller, J. B., et al. (2022). Estimating emissions of methane consistent with atmospheric measurements of methane and δ13C of methane. *Atmospheric Chemistry and Physics*, *22*(23), 15351–15377. https://doi.org/10.5194/acp-22-15351-2022

Cantrell, C. A., Shetter, R. E., McDaniel, A. H., Calvert, J. G., Davidson, J. A., Lowe, D. C., et al. (1990). Carbon kinetic isotope effect in the oxidation of methane by the hydroxyl radical. *Journal of Geophysical Research*, *95*(D13), 22455–22462. https://doi.org/10.1029/JD095iD13p22455

Chang, J., Peng, S., Ciais, P., Saunois, M., Dangal, S. R. S., Herrero, M., et al. (2019). Revisiting enteric methane emissions from domestic ruminants and their $\delta^{13}C_{CH4}$ source signature. *Nature Communications*, *10*(1), 1–14. https://doi.org/10.1038/s41467-019-11066-3

Crippa, M., Guizzardi, D., Banja, M., Solazzo, E., Muntean, M., Schaaf, E., et al. (2022). *CO_2 emissions of all world countries*, 2022 Report. EUR 31182 EN, Publications Office of the European Union, Luxembourg.

Crippa, M., Guizzardi, D., Muntean, M., Schaaf, E., Lo Vullo, E., Solazzo, E., et al. (2021). EDGAR v6.0 greenhouse gas emissions [Dataset]. *Joint Research Centre (JRC)*. http://data.europa.eu/89h/97a67d67-c62e-4826-b873-9d972c4f670b

Crippa, M., Solazzo, E., Huang, G., Guizzardi, D., Koffi, E., Muntean, M., et al. (2020). High resolution temporal profiles in the emissions database for global atmospheric research. *Earth System Science Data*, *7*(1), 121. https://doi.org/10.1038/s41597-020-0462-2

Dlugokencky, E. J., Crotwell, A. M., Mund, J. W., & Crotwell, M. J. (2021). Atmospheric methane dry air mole fractions from the NOAA GML carbon cycle cooperative global air sampling network, 1983-2020, version: 2021-07-30 [Dataset]. https://doi.org/10.15138/vncz-m766

Doucet, A., Freitas, N., & Gordon, N. (2001). *Sequential Monte Carlo methods in practice*. Springer.

Eisma, R., Vermeulen, A. T., & Van Der Borg, K. (1995). 14CH4 Emissions from nuclear power plants in Northwestern Europe. *Radiocarbon*, *37*(2), 475–483. https://doi.org/10.1017/s0033822200030952

Etiope, G., Ciotoli, G., Schwietzke, S., & Schoell, M. (2019). Gridded maps of geological methane emissions and their isotopic signature. *Earth System Science Data*, *11*(1), 1–22. https://doi.org/10.5194/essd-11-1-2019

Etiope, G., & Schwietzke, S. (2019). Global geological methane emissions: An update of top-down and bottom-up estimates. *Elementa: Science of the Anthropocene*, *7*(47). https://doi.org/10.1525/journal.elementa.383

Ferretti, D. F., Miller, J. B., White, J. W. C., Etheridge, D. M., Lassey, K. R., Lowe, D. C., et al. (2005). Unexpected changes to the global methane budget over the past 2000 years. *Science*, *309*(5741), 1714–1717. https://doi.org/10.1126/science.1115193

France, J. L., Lunt, M. F., Andrade, M., Moreno, I., Ganesan, A. L., Lachlan-Cope, T., et al. (2022). Very large fluxes of methane measured above Bolivian seasonal wetlands. *Proceedings of the National Academy of Sciences* (Vol. 119(32), e2206345119). https://doi.org/10.1073/pnas.2206345119

Fujita, R., Morimoto, S., Maksyutov, S., Kim, H. S., Arshinov, M., Brailsford, G., et al. (2020). Global and regional CH_4 emissions for 1995–2013 derived from atmospheric CH_4, $\delta^{13}C$-CH_4, and δD-CH_4 observations and a chemical transport model. *Journal of Geophysical Research: Atmospheres*, *125*(14). https://doi.org/10.1029/2020JD032903

Ganesan, A. L., Stell, A. C., Gedney, N., Comyn-Platt, E., Hayman, G., Rigby, M., et al. (2018). Spatially resolved isotopic source signatures of wetland methane emissions. *Geophysical Research Letters*, *45*(8), 3737–3745. https://doi.org/10.1002/2018gl077536

Gidden, M. J., Riahi, K., Smith, S. J., Fujimori, S., Luderer, G., Kriegler, E., et al. (2019). Global emissions pathways under different socio-economic scenarios for use in CMIP6: A dataset of harmonized emissions trajectories through the end of the century. *Geoscientific Model Development*, *12*(4), 1443–1475. https://doi.org/10.5194/gmd-12-1443-2019

Graven, H., Allison, C. E., Etheridge, D. M., Hammer, S., Keeling, R. F., Levin, I., et al. (2017). Compiled records of carbon isotopes in atmospheric CO_2 for historical simulations in CMIP6. *Geoscientific Model Development*, *10*(12), 4405–4417. https://doi.org/10.5194/gmd-10-4405-2017

Graven, H., & Gruber, N. (2011). Continental-scale enrichment of atmospheric $^{14}CO_2$ from the nuclear power industry: Potential impact on the estimation of fossil fuel-derived $^{14}CO_2$. *Atmospheric Chemistry and Physics*, *11*(23), 12339–12349. https://doi.org/10.5194/acp-11-12339-2011

Gromov, S., Brenninkmeijer, C. A. M., & Jöckel, P. (2018). A very limited role of tropospheric chlorine as a sink of the greenhouse gas methane. *Atmospheric Chemistry and Physics*, *18*(13), 9831–9843. https://doi.org/10.5194/acp-18-9831-2018

Hein, R., Crutzen, P. J., & Heimann, M. (1997). An inverse modeling approach to investigate the global atmospheric methane cycle. *Global Biogeochemical Cycles*, *11*(1), 43–76. https://doi.org/10.1029/96gb03043

Hmiel, B., Petrenko, V. V., Dyonisius, M. N., Buizert, C., Smith, A. M., Place, P. F., et al. (2020). Preindustrial $^{14}CH_4$ indicates greater anthropogenic fossil CH_4 emissions. *Nature*, *578*(7795), 409–412. https://doi.org/10.1038/s41586-020-1991-8

Hoesly, R. M., Smith, S. J., Feng, L., Klimont, Z., Janssens-Maenhout, G., Pitkanen, T., et al. (2018). Historical (1750–2014) anthropogenic emissions of reactive gases and aerosols from the Community Emissions Data System (CEDS). *Geoscientific Model Development*, *11*(1), 369–408. https://doi.org/10.5194/gmd-11-369-2018

Höglund-Isaksson, L., Gómez-Sanabria, A., Klimont, Z., Rafaj, P., & Schöpp, W. (2020). Technical potentials and costs for reducing global anthropogenic methane emissions in the 2050 timeframe –results from the GAINS model. *Environmental Research Communications*, *2*(2), 025004. https://doi.org/10.1088/2515-7620/ab7457

IAEA PRIS. (2017). Country statistics: The database of annual energy output for pressurized water reactors from international atomic energy Agency's power reactor information system. Retrieved from https://www.iaea.org/pris/(dateofaccess:30/10/2017)

IEA. (2022). *Global methane tracker 2022*. IEA. Retrieved from https://www.iea.org/reports/global-methane-tracker-2022,License:CCBY4.0

IPCC. (2021). In P. Zhai, A. Pirani, S. L. Connors, C. Péan, S. Berger, et al. (Eds.), *Climate change 2021: The physical science basis. Contribution of working group I to the sixth Assessment report of the intergovernmental panel on climate change Masson-Delmotte, V*. Cambridge University Press. 2391.

Janssens-Maenhout, G., Crippa, M., Guizzardi, D., Muntean, M., Schaaf, E., Dentener, F., et al. (2019). EDGAR v4.3.2 Global Atlas of the three major greenhouse gas emissions for the period 1970–2012. *Earth System Science Data*, *11*(3), 959–1002. https://doi.org/10.5194/essd-11-959-2019

Kitagawa, G. (1996). Monte Carlo filter and smoother for Non-Gaussian nonlinear state space models. *Journal of Computational & Graphical Statistics*, *5*(1), 1–25. https://doi.org/10.1080/10618600.1996.10474692

Kunz, C. (1985). Carbon-14 discharge at three light-water reactors. *Health Physics*, *49*(1), 25–35. https://doi.org/10.1097/00004032-198507000-00002

Lan, X., Basu, S., Schwietzke, S., Bruhwiler, L. M. P., Dlugokencky, E. J., Michel, S. E., et al. (2021). Improved constraints on global methane emissions and sinks using $\delta^{13}C$-CH_4. *Global Biogeochemical Cycles*, *35*(6). https://doi.org/10.1029/2021gb007000

Lassey, K. R., Etheridge, D. M., Lowe, D. C., Smith, A. M., & Ferretti, D. F. (2007). Centennial evolution of the atmospheric methane budget: What do the carbon isotopes tell us? *Atmospheric Chemistry and Physics*, *7*(8), 2119–2139. https://doi.org/10.5194/acp-7-2119-2007

Lassey, K. R., Lowe, D. C., & Smith, A. M. (2007). The atmospheric cycling of radiomethane and the "fossil fraction" of the methane source. *Atmospheric Chemistry and Physics*, *7*(8), 2141–2149. https://doi.org/10.5194/acp-7-2141-2007

Lauvaux, T., Giron, C., Mazzolini, M., d'Aspremont, A., Duren, R., Cusworth, D., et al. (2022). Global assessment of oil and gas methane ultra-emitters. *Science*, *375*(6580), 557–561. https://doi.org/10.1126/science.abj4351

Lu, X., Harris, S. J., Fisher, R. E., France, J. L., Nisbet, E. G., Lowry, D., et al. (2021). Isotopic signatures of major methane sources in the coal seam gas fields and adjacent agricultural districts, Queensland, Australia. *Atmospheric Chemistry and Physics*, *21*(13), 10527–10555. https://doi.org/10.5194/acp-21-10527-2021

Maasakkers, J. D., Jacob, D. J., Sulprizio, M. P., Scarpelli, T. R., Nesser, H., Sheng, J.-X., et al. (2019). Global distribution of methane emissions, emission trends, and OH concentrations and trends inferred from an inversion of GOSAT satellite data for 2010–2015. *Atmospheric Chemistry and Physics*, *19*(11), 7859–7881. https://doi.org/10.5194/acp-19-7859-2019

Manning, M. R., Lowe, D. C., Melhuish, W. H., Sparks, R. J., Wallace, G., Brenninkmeijer, C. A. M., & McGill, R. C. (1990). The use of radiocarbon measurements in atmospheric studies. *Radiocarbon*, *32*(1), 37–58. https://doi.org/10.1017/s0033822200039941

Meinshausen, M., Vogel, E., Nauels, A., Lorbacher, K., Meinshausen, N., Etheridge, D. M., et al. (2017). Historical greenhouse gas concentrations for climate modelling (CMIP6). *Geoscientific Model Development*, *10*(5), 2057–2116. https://doi.org/10.5194/gmd-10-2057-2017

Michel, S. E., Vaughn, B. H., Tans, P., Thoning, K., & Lan, X. (2021). *Atmospheric δ13C-CH4 data from the Institute of Arctic and Alpine Research (INSTAAR) at the University of Colorado*. Boulder in cooperation with NOAA Global Monitoring Laboratory. https://doi.org/10.15138/79jq-qc24

Mischler, J. A., Sowers, T. A., Alley, R. B., Battle, M., McConnell, J. R., Mitchell, L., et al. (2009). Carbon and hydrogen isotopic composition of methane over the last 1000 years. *Global Biogeochemical Cycles*, *23*(4). https://doi.org/10.1029/2009gb003460

Naus, S., Montzka, S. A., Pandey, S., Basu, S., Dlugokencky, E. J., & Krol, M. (2019). Constraints and biases in a tropospheric two-box model of OH. *Atmospheric Chemistry and Physics*, *19*(1), 407–424. https://doi.org/10.5194/acp-19-407-2019

Naus, S., Montzka, S. A., Patra, P. K., & Krol, M. C. (2021). A three-dimensional-model inversion of methyl chloroform to constrain the atmospheric oxidative capacity. *Atmospheric Chemistry and Physics*, *21*(6), 4809–4824. https://doi.org/10.5194/acp-21-4809-2021

Nicely, J. M., Canty, T. P., Manyin, M., Oman, L. D., Salawitch, R. J., Steenrod, S. D., et al. (2018). Changes in global tropospheric OH expected as a result of climate change over the last several decades. *Journal of Geophysical Research: Atmospheres*, *123*(18), 10–774. https://doi.org/10.1029/2018JD028388

MOYA/ZWAMPS Team, Nisbet, E. G., Allen, G., Fisher, R. E., France, J. L., Lee, J. D., et al. (2022). Isotopic signatures of methane emissions from tropical fires, agriculture and wetlands: The MOYA and ZWAMPS flights. *Philosophical transactions. Series A, Mathematical, physical, and engineering sciences*, *380*(2215), 20210112. https://doi.org/10.1098/rsta.2021.0112

Olivier, J. G. J., & Berdowski, J. J. M. (2001). Global emissions sources and sinks. In J. Berdowski, R. Guicherit, & B. J. Heij (Eds.), *The climate system* (pp. 33–78). A.A. Balkema Publishers/Swets and Zeitlinger Publishers.

O'Rourke, P. R., Smith, S. J., Mott, A., Ahsan, H., McDuffie, E. E., Crippa, M., et al. (2021). CEDS v_2021_04_21 Release emission data (v_2021_04_21) [Dataset]. https://doi.org/10.5281/zenodo.4741285

Pandey, S., Houweling, S., Lorente, A., Borsdorff, T., Tsivlidou, M., Bloom, A. A., et al. (2021). Using satellite data to identify the methane emission controls of South Sudan's wetlands. *Biogeosciences*, *18*(2), 557–572. https://doi.org/10.5194/bg-18-557-2021

Patra, P. K., Krol, M. C., Prinn, R. G., Takigawa, M., Mühle, J., Montzka, S. A., et al. (2021). Methyl chloroform continues to constrain the hydroxyl (OH) variability in the troposphere. *Journal of Geophysical Research: Atmospheres*, *126*(4). https://doi.org/10.1029/2020jd033862

Plant, G., Kort, E. A., Brandt, A. R., Chen, Y., Fordice, G., Gorchov Negron, A. M., et al. (2022). Inefficient and unlit natural gas flares both emit large quantities of methane. *Science*, *377*(6614), 1566–1571. https://doi.org/10.1126/science.abq0385

Prather, M. J., Holmes, C. D., & Hsu, J. (2012). Reactive greenhouse gas scenarios: Systematic exploration of uncertainties and the role of atmospheric chemistry. *Geophysical Research Letters*, *39*(9). https://doi.org/10.1029/2012gl051440

Quay, P., Stutsman, J., Wilbur, D., Snover, A., Dlugokencky, E., & Brown, T. (1999). The isotopic composition of atmospheric methane. *Global Biogeochemical Cycles*, *13*(2), 445–461. https://doi.org/10.1029/1998gb900006

RADD. (2017). The European commission radioactive discharges database [Dataset]. http://europa.eu/radd/nuclideDischargeOverview.dox?pageID=NuclideDischargeOverview

Reimer, P. J., Bard, E., Bayliss, A., Beck, J. W., Blackwell, P. G., Ramsey, C. B., et al. (2013). IntCal13 and Marine13 radiocarbon age Calibration Curves 0–50,000 Years Cal BP. *Radiocarbon*, *55*(4), 1869–1887. https://doi.org/10.2458/azu_js_rc.55.16947

Rice, A. L., Butenhoff, C. L., Teama, D. G., Roger, F. H., Khalil, M. A., & Rasmussen, R. A. (2016). Atmospheric methane isotopic record favors fossil sources flat in 1980s and 1990s with recent increase. *Proceedings of the National Academy of Sciences* (Vol. 113(39), 10791–10796). https://doi.org/10.1073/pnas.1522923113

Rigby, M., Montzka, S. A., Prinn, R. G., White, J. W. C., Young, D., O'Doherty, S., et al. (2017). Role of atmospheric oxidation in recent methane growth. *Proceedings of the National Academy of Sciences* (Vol. 114(21), 5373–5377). https://doi.org/10.1073/pnas.1616426114

Sargent, M. R., Floerchinger, C., McKain, K., Budney, J., Gottlieb, E. W., Hutyra, L. R., et al. (2021). Majority of US urban natural gas emissions unaccounted for in inventories. *Proceedings of the National Academy of Sciences* (Vol. 118(44)). https://doi.org/10.1073/pnas.2105804118

Saunois, M., Stavert, A. R., Poulter, B., Bousquet, P., Canadell, J. G., Jackson, R. B., et al. (2020). The global methane budget 2000–2017. *Earth System Science Data*, *12*(3), 1561–1623. https://doi.org/10.5194/essd-12-1561-2020

Scarpelli, T. R., Jacob, D. J., Grossman, S., Lu, X., Qu, Z., Sulprizio, M. P., et al. (2022). Updated Global Fuel Exploitation Inventory (GFEI) for methane emissions from the oil, gas, and coal sectors: Evaluation with inversions of atmospheric methane observations. *Atmospheric Chemistry and Physics*, *22*(5), 3235–3249. https://doi.org/10.5194/acp-22-3235-2022

Schaefer, H., Mikaloff Fletcher, S. E., Veidt, C., Lassey, K. R., Brailsford, G. W., Bromley, T. M., et al. (2016). A 21st-century shift from fossil-fuel to biogenic methane emissions indicated by $^{13}CH_4$. *Science*, *352*(6281), 80–84. https://doi.org/10.1126/science.aad2705

Schwietzke, S., Sherwood, O. A., Bruhwiler, L. M., Miller, J. B., Etiope, G., Dlugokencky, E. J., et al. (2016). Upward revision of global fossil fuel methane emissions based on isotope database. *Nature*, *538*(7623), 88–91. https://doi.org/10.1038/nature19797

Shaw, J. T., Allen, G., Barker, P., Pitt, J. R., Pasternak, D., Bauguitte, S. J. B., et al. (2022). Large methane emission fluxes observed from tropical wetlands in Zambia. *Global Biogeochemical Cycles*, *36*(6). https://doi.org/10.1029/2021gb007261

Shen, L., Jacob, D. J., Gautam, R., Omara, M., Scarpelli, T. R., Lorente, A., et al. (2023). National quantifications of methane emissions from fuel exploitation using high resolution inversions of satellite observations. *Nature Communications*, *14*(1), 4948. https://doi.org/10.1038/s41467-023-40671-6

Sherwood, O. A., Schwietzke, S., Arling, V. A., & Etiope, G. (2017). Global inventory of gas geochemistry data from fossil fuel, microbial and burning sources, version 2017. *Earth System Science Data*, *9*(2), 639–656. https://doi.org/10.5194/essd-9-639-2017

Sherwood, O. A., Schwietzke, S., & Lan, X. (2021). Global $\delta^{13}C\text{-}CH_4$ source signature inventory 2020.

Stevenson, D. S., Zhao, A., Naik, V., O'Connor, F. M., Tilmes, S., Zeng, G., et al. (2020). Trends in global tropospheric hydroxyl radical and methane lifetime since 1850 from AerChemMIP. *Atmospheric Chemistry and Physics*, *20*(21), 12905–12920. https://doi.org/10.5194/acp-20-12905-2020

Thanwerdas, J., Saunois, M., Berchet, A., Pison, I., Vaughn, B. H., Michel, S. E., & Bousquet, P. (2022). Variational inverse modeling within the community inversion framework v1.1 to assimilate $\delta^{13}C(CH_4)$ and CH_4: A case study with model LMDz-SACS. *Geoscientific Model Development*, *15*(12), 4831–4851. https://doi.org/10.5194/gmd-15-4831-2022

Turner, A. J., Frankenberg, C., Wennberg, P. O., & Jacob, D. J. (2017). Ambiguity in the causes for decadal trends in atmospheric methane and hydroxyl. *Proceedings of the National Academy of Sciences* (Vol. 114(21), 5367–5372). https://doi.org/10.1073/pnas.1616020114

Umezawa, T., Brenninkmeijer, C. A. M., Röckmann, T., van der Veen, C., Tyler, S. C., Fujita, R., et al. (2018). Interlaboratory comparison of $\delta^{13}C$ and δD measurements of atmospheric CH_4 for combined use of data sets from different laboratories. *Atmospheric Measurement Techniques*, *11*(2), 1207–1231. https://doi.org/10.5194/amt-11-1207-2018

van Aardenne, J. A., Dentener, F. J., Olivier, J. G. J., Goldewijk, C. G. M. K., & Lelieveld, J. (2001). A 1°×1° resolution data set of historical anthropogenic trace gas emissions for the period 1890-1990. *Global Biogeochemical Cycles*, *15*(4), 909–928. https://doi.org/10.1029/2000gb001265

van Herpen, M., Li, Q., Saiz-Lopez, A., Liisberg, J. B., Rockmann, T., Cuevas, C. A., et al. (2023). Photocatalytic chlorine atom production on mineral dust-sea spray aerosols over the North Atlantic. *Proceedings of the National Academy of Sciences* (Vol. 120(31), e2303974120). https://doi.org/10.1073/pnas.2303974120

van Marle, M. J. E., Kloster, S., Magi, B. I., Marlon, J. R., Daniau, A.-L., Field, R. D., et al. (2017). Historic global biomass burning emissions for CMIP6 (BB4CMIP) based on merging satellite observations with proxies and fire models (1750–2015). *Geoscientific Model Development*, *10*(9), 3329–3357. https://doi.org/10.5194/gmd-10-3329-2017

Wahlen, M., Tanaka, N., Henry, R., Deck, B., Zeglen, J., Vogel, J. S., et al. (1989). Carbon-14 in methane sources and in atmospheric methane: The contribution from fossil carbon. *Science*, *245*(4915), 286–290. https://doi.org/10.1126/science.245.4915.286

Warwick, N. J., Cain, M. L., Fisher, R., France, J. L., Lowry, D., Michel, S. E., et al. (2016). Using $\delta^{13}C\text{-}CH_4$ and $\delta D\text{-}CH_4$ to constrain Arctic methane emissions. *Atmospheric Chemistry and Physics*, *16*(23), 14891–14908. https://doi.org/10.5194/acp-16-14891-2016

White, J. W. C., Vaughn, B. H., & Michel, S. E. (2016). University of Colorado, Institute of Arctic and Alpine research (INSTAAR), stable isotopic composition of atmospheric methane (D/H) from the NOAA ESRL carbon cycle cooperative global air sampling network, 2005-2009, version: 2016-04-25 [Dataset]. ftp://aftp.cmdl.noaa.gov/data/trace_gases/ch4h2/flask/

Worden, J. R., Bloom, A. A., Pandey, S., Jiang, Z., Worden, H. M., Walker, T. W., et al. (2017). Reduced biomass burning emissions reconcile conflicting estimates of the post-2006 atmospheric methane budget. *Nature Communications*, *8*(1), 2227. https://doi.org/10.1038/s41467-017-02246-0

Zazzeri, G., Graven, H., Xu, X., Saboya, E., Blyth, L., Manning, A. J., et al. (2023). Radiocarbon measurements reveal underestimated fossil CH4 and CO2 emissions in London. *Geophysical Research Letters*, *50*(15), e2023GL103834. https://doi.org/10.1029/2023GL103834

Zazzeri, G., Xu, X., & Graven, H. (2021). Efficient sampling of atmospheric methane for radiocarbon analysis and quantification of fossil methane. *Environmental Science & Technology*, *55*(13), 8535–8541. https://doi.org/10.1021/acs.est.0c03300

Zazzeri, G., Yeomans, E. A., & Graven, H. D. (2018). Global and regional emissions of radiocarbon from nuclear power plants from 1972 to 2016. *Radiocarbon*, *60*(4), 1067–1081. https://doi.org/10.1017/rdc.2018.42

References From the Supporting Information

Allan, W., Struthers, H., & Lowe, D. C. (2007). Methane carbon isotope effects caused by atomic chlorine in the marine boundary layer: Global model results compared with Southern Hemisphere measurements. *Journal of Geophysical Research*, *112*(D4). https://doi.org/10.1029/2006jd007369

Beck, J., Bock, M., Schmitt, J., Seth, B., Blunier, T., & Fischer, H. (2018). Bipolar carbon and hydrogen isotope constraints on the Holocene methane budget. *Biogeosciences*, *15*(23), 7155–7175. https://doi.org/10.5194/bg-15-7155-2018

Cao, M., Marshall, S., & Gregson, K. (1996). Global carbon exchange and methane emissions from natural wetlands: Application of a process-based model. *Journal of Geophysical Research*, *101*(D9), 14399–14414. https://doi.org/10.1029/96jd00219

Craig, H. (1957). Isotopic standards for carbon and oxygen and correction factors for mass-spectrometric analysis of carbon dioxide. *Geochimica et Cosmochimica Acta*, *12*(1), 133–149. https://doi.org/10.1016/0016-7037(57)90024-8

DeMore, W. B. (1993). Rate constant ratio for the reactions of OH with CH_3D and CH_4. *Journal of Physical Chemistry*, *97*(33), 8564–8566. https://doi.org/10.1021/j100135a006

Gierczak, T., Talukdar, R. K., Herndon, S. C., Vaghjiani, G. L., & Ravishankara, A. R. (1997). Rate coefficients for the reactions of hydroxyl radicals with methane and deuterated methanes. *The Journal of Physical Chemistry A*, *101*(17), 3125–3134. https://doi.org/10.1021/jp963892r

Hagemann, R., Nief, G., & Roth, E. (1970). Absolute isotopic scale for deuterium analysis of natural waters. Absolute D/H ratio for SMOW. *Tellus*, *22*(6), 712–715. https://doi.org/10.1111/j.2153-3490.1970.tb00540.x

Ito, A. (2021). Output data of greenhouse gas budget and carbon cycle simulated by the VISIT terrestrial ecosystem model. ver.2021. *NIES*, *1*. https://doi.org/10.17595/20210521.001

Joelsson, L. M. T., Schmidt, J. A., Nilsson, E. J. K., Blunier, T., Griffith, D. W. T., Ono, S., & Johnson, M. S. (2016). Kinetic isotope effects of $^{12}CH_3D + OH$ and $^{13}CH_3D + OH$ from 278 to 313 K. *Atmospheric Chemistry and Physics*, *16*(7), 4439–4449. https://doi.org/10.5194/acp-16-4439-2016

Nakazawa, T., Ishizawa, M., Higuchi, K. A. Z., & Trivett, N. B. A. (1997). Two curve fitting methods applied to CO_2 flask data. *Environmetrics*, *8*(3), 197–218. https://doi.org/10.1002/(sici)1099-095x(199705)8:3<197::Aid-env248>3.0.Co;2-c

Paudel, R., Mahowald, N. M., Hess, P. G. M., Meng, L., & Riley, W. J. (2016). Attribution of changes in global wetland methane emissions from pre-industrial to present using CLM4.5-BGC. *Environmental Research Letters*, *11*(3), 034020. https://doi.org/10.1088/1748-9326/11/3/034020

Poulter, B., Bousquet, P., Canadell, J. G., Ciais, P., Peregon, A., Saunois, M., et al. (2017). Global wetland contribution to 2000–2012 atmospheric methane growth rate dynamics. *Environmental Research Letters*, *12*(9), 094013. https://doi.org/10.1088/1748-9326/aa8391

Reeburgh, W. S., Hirsch, A. I., Sansone, F. J., Popp, B. N., & Rust, T. M. (1997). Carbon kinetic isotope effect accompanying microbial oxidation of methane in boreal forest soils. *Geochimica et Cosmochimica Acta*, *61*(22), 4761–4767. https://doi.org/10.1016/s0016-7037(97)00277-9

Rice, A. L., Tyler, S. C., McCarthy, M. C., Boering, K. A., & Atlas, E. (2003). Carbon and hydrogen isotopic compositions of stratospheric methane: 1. High-Precision observations from the NASA ER-2 aircraft. *Journal of Geophysical Research*, *108*(D15). https://doi.org/10.1029/2002jd003042

Röckmann, T., Brass, M., Borchers, R., & Engel, A. (2011). The isotopic composition of methane in the stratosphere: High-altitude balloon sample measurements. *Atmospheric Chemistry and Physics*, *11*(24), 13287–13304. https://doi.org/10.5194/acp-11-13287-2011

Sapart, C. J., Martinerie, P., Witrant, E., Chappellaz, J., van de Wal, R. S. W., Sperlich, P., et al. (2013). Can the carbon isotopic composition of methane be reconstructed from multi-site firn air measurements? *Atmospheric Chemistry and Physics*, *13*(14), 6993–7005. https://doi.org/10.5194/acp-13-6993-2013

Saueressig, G., Bergamaschi, P., Crowley, J. N., Fischer, H., & Harris, G. W. (1995). Carbon kinetic isotope effect in the reaction of CH_4 with Cl atoms. *Geophysical Research Letters*, *22*(10), 1225–1228. https://doi.org/10.1029/95GL00881

Saueressig, G., Bergamaschi, P., Crowley, J. N., Fischer, H., & Harris, G. W. (1996). D/H kinetic isotope effect in the reaction CH_4+Cl. *Geophysical Research Letters*, *23*(24), 3619–3622. https://doi.org/10.1029/96gl03292

Saueressig, G., Crowley, J. N., Bergamaschi, P., Brühl, C., Brenninkmeijer, C. A. M., & Fischer, H. (2001). Carbon 13 and D kinetic isotope effects in the reactions of CH_4 with $O(^1D)$ and OH: New laboratory measurements and their implications for the isotopic composition of stratospheric methane. *Journal of Geophysical Research*, *106*(D19), 23127–23138. https://doi.org/10.1029/2000jd000120

Schmitt, J., Seth, B., Bock, M., van der Veen, C., Möller, L., Sapart, C. J., et al. (2013). On the interference of Kr during carbon isotope analysis of methane using continuous-flow combustion–isotope ratio mass spectrometry. *Atmospheric Measurement Techniques*, *6*(5), 1425–1445. https://doi.org/10.5194/amt-6-1425-2013

Snover, A. K., & Quay, P. D. (2000). Hydrogen and carbon kinetic isotope effects during soil uptake of atmospheric methane. *Global Biogeochemical Cycles*, *14*(1), 25–39. https://doi.org/10.1029/1999gb900089

Stuiver, M. (1980). Workshop on 14C data reporting. *Radiocarbon*, *22*(3), 964–966. https://doi.org/10.1017/s0033822200010389

Swart, N. C., Cole, J. N. S., Kharin, V. V., Lazare, M., Scinocca, J. F., Gillett, N. P., et al. (2019). The Canadian Earth system model version 5 (CanESM5.0.3). *Geoscientific Model Development*, *12*(11), 4823–4873. https://doi.org/10.5194/gmd-12-4823-2019

Tyler, S. C., Ajie, H. O., Rice, A. L., Cicerone, R. J., & Tuazon, E. C. (2000). Experimentally determined kinetic isotope effects in the reaction of CH_4 with Cl: Implications for atmospheric CH_4. *Geophysical Research Letters*, *27*(12), 1715–1718. https://doi.org/10.1029/1999gl011168

Tyler, S. C., Crill, P. M., & Brailsford, G. W. (1994). Fractionation of methane during oxidation in a temperate forested soil. *Geochimica et Cosmochimica Acta*, *58*(6), 1625–1633. https://doi.org/10.1016/0016-7037(94)90564-9

Walter, B. P., & Heimann, M. (2000). A process-based, climate-sensitive model to derive methane emissions from natural wetlands: Application to five wetland sites, sensitivity to model parameters, and climate. *Global Biogeochemical Cycles*, *14*(3), 745–765. https://doi.org/10.1029/1999gb001204

Waugh, D., & Hall, T. (2002). Age of stratospheric air: Theory, observations, and models. *Reviews of Geophysics*, *40*(4). https://doi.org/10.1029/2000rg000101